



## King's Research Portal

DOI:

[10.1002/mrm.27694](https://doi.org/10.1002/mrm.27694)

*Document Version*

Peer reviewed version

[Link to publication record in King's Research Portal](#)

*Citation for published version (APA):*

Bustin, A., Cruz, G., Jaubert, O., Lopez Gonzalez, K., Botnar, R., & Prieto, C. (2019). High-dimensionality undersampled patch-based reconstruction (HD-PROST) for accelerated multi-contrast MRI: HD-PROST reconstruction for accelerated multi-contrast MRI. *Magnetic Resonance in Medicine*, 81(6), 3705-3719. Advance online publication. <https://doi.org/10.1002/mrm.27694>

### **Citing this paper**

Please note that where the full-text provided on King's Research Portal is the Author Accepted Manuscript or Post-Print version this may differ from the final Published version. If citing, it is advised that you check and use the publisher's definitive version for pagination, volume/issue, and date of publication details. And where the final published version is provided on the Research Portal, if citing you are again advised to check the publisher's website for any subsequent corrections.

### **General rights**

Copyright and moral rights for the publications made accessible in the Research Portal are retained by the authors and/or other copyright owners and it is a condition of accessing publications that users recognize and abide by the legal requirements associated with these rights.

- Users may download and print one copy of any publication from the Research Portal for the purpose of private study or research.
- You may not further distribute the material or use it for any profit-making activity or commercial gain
- You may freely distribute the URL identifying the publication in the Research Portal

### **Take down policy**

If you believe that this document breaches copyright please contact [librarypure@kcl.ac.uk](mailto:librarypure@kcl.ac.uk) providing details, and we will remove access to the work immediately and investigate your claim.

1                   **High-Dimensionality Undersampled Patch-Based**  
 2                   **Reconstruction (HD-PROST) for Accelerated Multi-**  
 3                   **Contrast Magnetic Resonance Imaging**

4                   Aurélien Bustin<sup>1\*</sup>, Gastao Cruz<sup>1\*</sup>, Olivier Jaubert<sup>1</sup>, Karina Lopez<sup>1</sup>, René M.  
 5   Botnar<sup>1,2</sup>, Claudia Prieto<sup>1,2</sup>

6                   <sup>1</sup>Department of Biomedical Engineering, School of Imaging Sciences & Biomedical Engineering, King's  
 7   College London, King's Health Partners, London, United Kingdom

8   <sup>2</sup>Escuela de Ingeniería, Pontificia Universidad Católica de Chile,  
 9   Santiago, Chile

12  
 13  
 14  
 15  
 16 Short Title: HD-PROST reconstruction for accelerated multi-contrast MRI  
 17 Submitted as Full Paper to Magnetic Resonance in Medicine  
 18 Main document word count: 5036

19  
 20 \* Aurélien Bustin and Gastao Cruz contributed equally to this study

21  
 22  
 23 **Corresponding author:**

24	Name	Aurélien Bustin, PhD
25	Department	Department of Biomedical Engineering
26		School of Imaging Sciences & Biomedical Engineering
27	Institute	King's Health Partners, King's College London
28	Address	3 <sup>rd</sup> Floor, Lambeth Wing, St Thomas' Hospital
29		London SE1 7EH
30		United Kingdom
31	E-mail	aurelien.bustin@kcl.ac.uk

## ABSTRACT

35

36 **Purpose:** To develop a new high-dimensionality undersampled patch-based reconstruction  
37 (HD-PROST) for highly accelerated two-dimensional (2D) and three-dimensional (3D)  
38 multi-contrast magnetic resonance (MR) imaging.

39 **Methods:** HD-PROST jointly reconstructs multi-contrast MR images by exploiting the  
40 highly redundant information, on a local and non-local scale, and the strong correlation  
41 shared between the multiple contrast images. This is achieved by enforcing multi-  
42 dimensional low-rank in the undersampled images. 2D magnetic resonance fingerprinting  
43 (MRF) phantom and in vivo brain acquisitions were performed to evaluate the performance  
44 of HD-PROST for highly-accelerated simultaneous  $T_1$  and  $T_2$  mapping. Additional in vivo  
45 experiments for reconstructing multiple undersampled 3D Magnetization Transfer (MT)-  
46 weighted images were conducted to illustrate the impact of HD-PROST for high-resolution  
47 multi-contrast 3D imaging.

48 **Results:** In the 2D MRF phantom study, HD-PROST provided accurate and precise  
49 estimation of the  $T_1$  and  $T_2$  values in comparison to gold standard spin echo acquisitions.  
50 HD-PROST achieved good quality maps for the in vivo 2D MRF experiments in  
51 comparison to conventional low-rank inversion reconstruction.  $T_1$  and  $T_2$  values of white  
52 matter and grey matter were in good agreement with those reported in the literature for  
53 MRF acquisitions with reduced number of time-point images (500 time-point images,  
54  $\sim 2.5$ sec scan time). For in vivo MT-weighted 3D acquisitions (6 different contrasts), HD-  
55 PROST achieved similar image quality than the fully-sampled reference image for an  
56 undersampling factor of 6.5-fold.

57 **Conclusion:** HD-PROST enables multi-contrast 2D and 3D MR images in a short  
58 acquisition time without compromising image quality. Ultimately, this technique may  
59 increase the potential of conventional parameter mapping.

60 **Keywords:** multi-contrast MRI; MR fingerprinting; patch-based reconstruction; low-rank  
61 tensor decomposition; compressed-sensing, magnetization transfer contrast



## 63 **Introduction**

64 In Magnetic Resonance Imaging (MRI), multiple contrasts are exploited to extract  
65 clinically relevant tissue parameters and pathological tissue changes. These multiple  
66 contrasts are achieved using different imaging sequences and preparation pulses. Multi-  
67 contrast acquisitions also find important applications in parameter mapping (e.g.  $T_1$  and  $T_2$   
68 mapping) and magnetic resonance fingerprinting (MRF) (1,2). However these acquisitions  
69 lead to long scan times since multiple images with different contrasts need to be acquired,  
70 making parameter imaging more sensitive to physiological motion (3–6).

71 Parallel imaging (PI) (7–11), compressed sensing (CS) (12,13), as well as the combination  
72 of both undersampled reconstruction techniques (14,15) have been proposed to overcome  
73 the long scan times associated with multi-contrast imaging and parameter mapping. PI can  
74 accelerate multi-contrast imaging by undersampling each individual image and exploiting  
75 the information provided by multiple coil arrays, yet at a signal-to-noise ratio (SNR)  
76 penalty generally marked for high acceleration factors. Sparse CS alone has been shown to  
77 cope with the problem of undersampling through the use of random or pseudo-random  
78 sampling patterns and efficient regularized reconstructions which make the assumption that  
79 the multi-contrast images share common and sparse information in a specific domain (16–  
80 21). Even though these strategies have achieved acceleration factors that have not  
81 previously been possible to attain with parallel imaging alone, CS-based techniques still  
82 suffer from residual aliasing artifacts for high acceleration factors, which compromise the  
83 diagnostic value of the reconstructed multi-contrast images.

84 Recently, novel techniques that exploit the strong anatomical correlations observed in the  
85 contrast dimension (or parameter dimension) on a global or local scale have been proposed.  
86 Indeed, the nature of signal evolution in multi-contrast acquisitions exhibits a low-rank  
87 structure in the contrast dimension which can be exploited to further reduce scan times  
88 (17,22–24). These types of reconstruction techniques, also known as the globally (GLR) or  
89 locally low-rank (LLR) methods (25), have been efficiently used in many applications such  
90 as  $T_2$  mapping (26) or dynamic contrast enhanced MRI (27). More recently, high-order

91 tensor decomposition techniques, exploiting global correlation, have been efficiently  
92 employed to allow for highly accelerated multi-dimensional cardiac MRI acquisitions  
93 (28,29). While those techniques have shown promise for motion-resolved quantitative  
94 cardiac imaging by efficiently solving a global low-rank tensor decomposition, they do not  
95 exploit the strong non-local correlations between neighboring patches.

96 Motivated by the LLR techniques which exploit localized correlations in the contrast  
97 dimension, patch-based image reconstructions exploiting non-local spatial redundancies  
98 and low-rank matrix structures have been introduced for single-contrast MRI reconstruction  
99 to lead to even sparser representation (30,31). By modeling the similarity of image patches  
100 through block-matching, low-rank representation and filtering, two-dimensional (2D) (32)  
101 and three-dimensional (3D) (33) patch-based reconstructions have been shown to  
102 outperform conventional CS reconstructions by recovering better image details and edges  
103 and exhibiting better overall image quality.

104 In this study, we present a new reconstruction technique for highly accelerated 2D and 3D  
105 multi-channel multi-contrast MRI which combines the promising performances of patch-  
106 based reconstructions and the potential of low-rank image reconstruction through higher-  
107 order tensor decomposition. The proposed High-Dimensionality undersampled Patch-based  
108 RecOnSTruction (HD-PROST) technique is first applied to accelerated 2D radial MRF, for  
109 various acceleration factors, where a high degree of inherent redundancy can be exploited  
110 locally, non-locally and through the contrast dimension. In a second application, HD-  
111 PROST is employed to acquire multiple undersampled high-resolution 3D Cartesian  
112 Magnetization Transfer Contrast (MTC) images with several MT weightings in a reduced  
113 scan time.

114

## 115 **Theory**

116 The framework presented hereafter jointly reconstructs multi-channel multi-contrast  
117 images from undersampled 2D or 3D MR acquisitions. This is achieved by generalizing

118 our previously proposed PROST technique (33) to high dimensional imaging. A description  
 119 of the proposed HD-PROST reconstruction is presented, followed by the description of two  
 120 multi-contrast applications (2D radial and 3D Cartesian) where high-dimensionality can be  
 121 exploited to reduce acquisition time, which is often a key factor for clinical translation.

122 ***High-Dimensionality undersampled Patch-based RecOnStrucTion (HD-PROST)***

123 Let  $X \in \mathbb{C}^{M_x \times M_y \times M_z \times L}$  be the multi-contrast complex images that we seek to reconstruct,  
 124 where  $M_x$ ,  $M_y$  and  $M_z$  are the number of voxels in the  $x$ ,  $y$  and  $z$  spatial directions, and  $L$   
 125 is the number of contrast-weighted images. The corresponding complex receive-coil  
 126 sensitivity maps for the  $N_c$  channels are denoted as  $S \in \mathbb{C}^{M_x \times M_y \times M_z \times N_c}$ . Let  $Y \in \mathbb{C}^{Z \times L \times N_c}$   
 127 be the undersampled k-space data (with  $Z \ll M_x \times M_y \times M_z$ ). The joint multi-contrast  
 128 undersampled reconstruction can be combined with parallel imaging and cast as the  
 129 following inverse problem:

$$\operatorname{argmin}_X \frac{1}{2} \|AFSX - Y\|_F^2 \quad [1]$$

130 where  $A$  is the undersampling operator that acquires k-space data for each contrast-  
 131 weighted image,  $F$  denotes the Fourier transform operator and  $\|\cdot\|_F$  is the Frobenius norm.  
 132 Mathematically, this inverse problem is ill-posed, in the sense that the exact solution might  
 133 not exist or not be unique, making precise recovery of  $X$  hardly possible, and prior  
 134 assumptions on the unknown solution  $X$  have to be considered.

135 The principle behind HD-PROST reconstruction assumes that a multi-contrast image  $X$  can  
 136 be expressed as a high-order low-rank representation on a patch scale, with respect to an  
 137 appropriately chosen patch selection operator. The recovery problem can be formulated as  
 138 the following constrained optimization on the high-order low-rank tensor  $\mathcal{T}$ :

$$\operatorname{argmin}_X \frac{1}{2} \|AFSX - Y\|_F^2 + \sum_p \lambda_p \|\mathcal{T}_p\|_* \quad s. t. \quad \mathcal{T}_p = P_p(X) \quad [2]$$

139 where  $\lambda_p$  is the nonnegative sparsity-promoting regularization parameter and  $\|\cdot\|_*$  is the  
 140 nuclear norm that enforces multi-dimensional low-rank on a multi-contrast patch scale. The  
 141 patch selection operator  $P_p(\cdot)$  forms a 3D tensor from a patch centered at pixel  $p$  from a set  
 142 of multi-contrast images (see optimization 2 below). Now considering the constraint  $\mathcal{T}_p =$   
 143  $P_p(X)$ , and the encoding operator  $E = AFS$ , we can form the unconstrained Lagrangian of  
 144 Equation 2 by linearly combining the constraint and cost function (31,33):

$$\begin{aligned}
 & \mathcal{L}_{HD-PROST}(X, \mathcal{T}, b) : \\
 & = \operatorname{argmin}_{X, \mathcal{T}, b} \frac{1}{2} \|EX - Y\|_F^2 + \sum_p \lambda_p \|\mathcal{T}_p\|_* \\
 & + \frac{\mu}{2} \sum_p \left\| \mathcal{T}_p - P_p(X) - \frac{b_p}{\mu} \right\|_F^2
 \end{aligned} \tag{3}$$

145 where  $b$  is the Lagrange multiplier, and  $\mu > 0$  is the penalty parameter. Equation 3 can be  
 146 efficiently solved through operator-splitting via alternating direction method of multipliers  
 147 (ADMM) (34). ADMM simplifies the optimization process by alternating the minimization  
 148 with respect to the multi-contrast set of images  $X$  (optimization 1) and the high-order tensor  
 149  $\mathcal{T}$  (optimization 2) followed by an update of the augmented multiplier  $b$ , and repeating  
 150 these three steps until a convergence criterion is satisfied.

#### 151 *Optimization 1: Joint MR reconstruction update*

152 The first sub-problem is a joint multi-contrast MR reconstruction that incorporates the  
 153 denoised tensor  $\mathcal{T}$  (obtained at the end of optimization 2) as prior information in a parallel  
 154 imaging fashion to obtain  $X$ :

$$\mathcal{L}_{JointRecon}(X) := \operatorname{argmin}_X \frac{1}{2} \|EX - Y\|_F^2 + \frac{\mu}{2} \left\| \mathcal{T} - X - \frac{b}{\mu} \right\|_F^2 \tag{4}$$

155 Equation 4 corresponds to a standard iterative SENSE reconstruction with Tikhonov  
 156 regularization, where the solution  $X$  can be efficiently computed using the Conjugate  
 157 Gradient (35) algorithm.



158 *Optimization 2: High Order Singular Value Decomposition (HOSVD)-based denoising*

159 Considering the variable  $\tilde{\mathcal{T}}_p = P_p(X) + \frac{b_p}{\mu}$ , the second sub-problem minimizes with respect  
 160 to the high-order tensor  $\mathcal{T}$  and is given by

$$\mathcal{L}_{Tensor}(\mathcal{T}) := \operatorname{argmin}_{\mathcal{T}} \sum_p \frac{2\lambda_p}{\mu} \|\mathcal{T}_p\|_* + \sum_p \|\mathcal{T}_p - \tilde{\mathcal{T}}_p\|_F^2 \quad [5]$$

161  $X$  denotes multiple MR images with different contrasts. Several observations can be made  
 162 about  $X$ : 1) on a local scale, voxels at a specific location for a given contrast exhibit similar  
 163 intensity to their nearest neighbors (within a patch); 2) on a non-local scale, images for a  
 164 given contrast contain self-repeating patterns (measured as patch similarity within a  
 165 neighborhood); and 3) on a contrast scale, common structures and features are shared across  
 166 multiple contrast images. Motivated by these observations, the proposed joint multi-  
 167 channel multi-contrast problem can be cast as a multi-dimensional low-rank reconstruction.  
 168 Bearing this in mind, equation 5 can be solved on a multi-contrast patch level. The  
 169 construction of the high-order tensor  $\mathcal{T}$  is performed as a three-step process:

170 **Step 1** – Similar overlapping patches in  $X + \frac{b}{\mu}$  are grouped together to form a third-order  
 171 tensor: considering a  $3D + L$  reference patch of size  $N_x \times N_y \times N_z \times L$ , we build a high  
 172 dimensional tensor  $\tilde{\mathcal{T}}_p \in \mathbb{C}^{N \times K \times L}$  of  $K - 1$  similar  $3D + L$  patches, with  $N =$   
 173  $N_x \times N_y \times N_z$  (see Figure 1 – ‘unfolding’ and ‘tensor stacking’). A fixed local window  
 174 is used for the patch search while the contrast signature remains unchanged. Along this  
 175 line, the proposed reconstruction can exploit as much of the contrast and spatial  
 176 correlations as possible.

177 **Step 2** – The tensor  $\tilde{\mathcal{T}}_p$  exhibits a strong low multilinear rank structure and can therefore  
 178 be compressed into a tensor of smaller size (i.e. the core tensor) through tensor  
 179 decomposition (see Supporting Information Table S1 and Figure 1 – ‘High-Order  
 180 Tensor Decomposition’). The dominant components of the core tensor can be extracted  
 181 by computing a complex-valued higher-order singular value decomposition (HOSVD)

182 (36,37) and by only keeping the largest (given by the thresholding parameter  $\frac{2\lambda_p}{\mu}$ )  
 183 multilinear singular vectors and high-order singular values. This step effectively acts as  
 184 a high-order denoising process where the small discarded coefficients mainly reflect  
 185 contributions from noise and noise-like artifacts.

186 **Step 3** – The denoised tensor  $\mathcal{T}_p$  is then rearranged to form the denoised patches. Steps  
 187 1-3 are repeated over all patches in the image in a sliding window fashion. Since a single  
 188 patch might belong to several groups in step 1, the final denoised multi-contrast  
 189 complex-valued images  $\mathcal{T}$  are obtained by averaging (Figure 1 – ‘Aggregation’) the  
 190 different estimates.

191 The solution  $\mathcal{T}$  to this optimization problem is a denoised version of  $\tilde{\mathcal{T}}$  that is incorporated  
 192 in the optimization 1 as prior knowledge, as described before. The Lagrangian multiplier  $b$   
 193 is then updated and optimizations 1 and 2 are processed iteratively to improve the quality  
 194 of the reconstructed images. In the spirit of reproducible research, codes and examples for  
 195 the proposed HD-PROST technique are made available at  
 196 <http://www.kclcardiacmr.com/downloads/>.

197 The generalized reconstruction framework described before considers 2D or 3D Cartesian  
 198 multi-contrast acquisitions (as the 3D undersampled Cartesian multi MT-weighted  
 199 acquisitions considered in this study). Slight modifications in the reconstruction process  
 200 are required for the accelerated non-Cartesian 2D MRF application considered in this study  
 201 and will be described in the next section.

### 202 ***HD-PROST for Accelerated 2D Radial Parameter Mapping with MRF***

203 MRF (1) is a novel quantitative MRI approach that allows the simultaneous acquisition of  
 204 multi-parametric maps (e.g.  $T_1$ ,  $T_2$ ,  $M_0$ ) in a single efficient scan. Conventional MRF  
 205 sequences acquire in the order of thousand highly-undersampled time-point images by  
 206 pseudo-randomly collecting the MR data in a continuous fashion with time-varying  
 207 acquisition parameters (e.g. repetition time, flip angle). The spatial and temporal  
 208 incoherencies provide a unique signal evolution (or fingerprint) for each tissue. These

209 unique fingerprints can be matched, through pattern matching, to a pre-generated MRF  
 210 dictionary representative of the MRF sequence, and whose atoms are composed of  
 211 simulated signal evolution curves. This matching process is performed on a voxel-by-voxel  
 212 basis to identify the underlying tissue properties and generate quantitative parameter maps.  
 213 The highly-undersampled pseudo-random MRF acquisition results in a high level of noise  
 214 and aliasing in the reconstructed time-point images. Several iterative techniques have been  
 215 recently proposed to improve the reconstruction quality of each time-point image (38–42).  
 216 Zhao et al. proposed to enforce low-rank and subspace modeling in the temporal dimension  
 217 to reconstruct high-quality time-point images (38). Assländer et al. recently introduced a  
 218 low-rank ADMM reconstruction technique to temporally compress the time-point images,  
 219 resulting in a reduced number of singular value images. The reconstruction of the  
 220 temporally compressed images is faster and better posed than reconstructing each time-  
 221 point image separately (39). This temporal compression operator  $U_r$  is obtained through  
 222 compression of the MRF dictionary at an appropriate rank  $r$ . Due to the multi-contrast  
 223 nature of MRF, HD-PROST can be used to explicitly exploit the local, non-local and  
 224 contrast information of the temporally compressed images by integrating the compression  
 225 operator into the encoding operator in Equation 3 as follows:

$$E_{MRF} = AU_rFS \quad [6]$$

## 226 **Methods**

227 The proposed HD-PROST reconstruction was evaluated on accelerated radial 2D MRF  
 228 phantom and in vivo brain acquisitions, and on accelerated Cartesian 3D magnetization  
 229 transfer imaging with varying MT-weighting in in vivo brain data. The two applications are  
 230 described in detail below along with imaging and reconstruction parameters. Written  
 231 informed consent was obtained from all subjects before undergoing MRI scans and the  
 232 study was approved by the Institutional Review Board.

## 233 **Accelerated 2D Magnetic Resonance Fingerprinting**

234 MRF acquisitions were performed on a 1.5T Ingenia MR system (Philips, Best, The  
235 Netherlands) equipped with a 15-element head coil.

### 236 *Phantom and In Vivo Experiments*

237 A 2D MRF acquisition was performed on a standardized (TIMES)  $T_1/T_2$  phantom  
238 containing nine agarose-based tubes with different  $T_1$  and  $T_2$  combinations (range,  $T_1$ : 255  
239 ms to 1489 ms,  $T_2$ : 44 ms to 243 ms) (43). Relevant scan parameters included: balanced  
240 steady-state free precession radial sequence, echo time (TE) = 2 ms, fixed repetition time  
241 (TR) = 4.4 ms, field-of-view (FOV) = 160x160 mm<sup>2</sup>, in-plane resolution = 1x1 mm<sup>2</sup>, slice  
242 thickness = 8 mm, bandwidth = 723.4 Hz/pixel. Only one radial spoke was acquired at each  
243 time-point (resulting in an acceleration factor of about 251 with respect to a fully-sampled  
244 radial acquisition). A total of 2000 time-points were acquired in 10 seconds. A flip angle  
245 (FA) pattern similar to the one proposed in (44) for optimized  $T_1/T_2$  mapping was used, and  
246 is shown in Supporting Information Figure S1. This RF pattern, which has been shown to  
247 be optimal in a Cramér-Rao lower bound sense, consists of intrinsic repetitive loops which  
248 offers the advantage to lengthen the scan time by simple concatenation. The experiments  
249 consisted of undersampling the acquired data by keeping only [1:  $n$ ] k-space radial spokes,  
250 with  $n = [400: 100: 2000]$ , resulting in scan time reductions up to a factor of 5 with respect  
251 to the 2000 time-points sequence.

252 Reference  $T_1$  and  $T_2$  times for each vial were obtained from gold standard spin echo (SE)  
253 acquisitions. For  $T_1$  values, an inversion-recovery SE (IRSE) sequence was used with eight  
254 inversion times from 25 ms to 3200 ms with TR = 10s, TE = 14.75ms. For  $T_2$  values, the  
255 SE sequence was performed with eight TEs from 10 ms to 640 ms.  $T_1$  and  $T_2$  values were  
256 obtained by mono-exponential curve fitting.

257 Single slice 2D MRF brain data were acquired in five healthy subjects (four men, mean  
258 age: 32 years; range: 28-37 years) using the same scan parameters as in the phantom  
259 experiments.

### 260 *Image Reconstruction*

261 For both phantom and in vivo 2D MRF experiments, data was temporally compressed with  
 262  $r = 10$ , leading to only 10 singular value images to reconstruct (i.e. in this study,  $L = 10$   
 263 and  $M_z = 1$ ).

264 HD-PROST reconstruction was implemented using the algorithm described in Supporting  
 265 Information Table S2 and performed offline on a workstation with a 16-core Dual Intel  
 266 Xeon Processor (23 GHz, 256 GB RAM). The joint MR reconstruction step (optimization  
 267 1) was implemented in Matlab (v7.1, MathWorks, Natick, MA) and the multi-contrast  
 268 patch-based denoising step (optimization 2) in C++. Coil sensitivity maps were estimated  
 269 using the eigenvalue-based approach ESPIRiT (45).

270 The encoding operator  $E_{MRF}$  was implemented using the nonuniform fast Fourier transform  
 271 (46). The tolerance of the conjugate gradient was set to  $CG_{eps} = 1e^{-4}$  and a maximum  
 272 number of  $CG_{iter} = 15$  iterations was chosen as stopping criterion. The regularization  
 273 parameter  $\mu$ , which balances the contribution of the prior term (obtained at the end of  
 274 optimization 2) and the data fidelity term, was set to  $5e^{-3}$ .

275 The proposed high-order patch-based denoising strategy was implemented as described in  
 276 Supporting Information Table S1. The performance of the proposed strategy relies on the  
 277 optimal selection of several parameters. The patch size, which controls the degree of local  
 278 image features, was set to  $N = 7 \times 7$ . We set the search window radius around each pixel  
 279 to 20 and restricted the number of similar patches selected to  $K = 20$  to form a third-order  
 280 tensor  $\mathcal{T}_p$  of size  $49 \times 20 \times 10$ . The  $l_2$  distance was chosen as measure of patch similarity  
 281 and was defined as  $d(patch_{ref}, patch_j) = \|patch_{ref} - patch_j\|_2$  for  $j = 1, \dots, K - 1$ . In  
 282 order to save computational complexity, a sliding-window approach was performed with a  
 283 patch offset of 3 pixels at each image dimension. The performance of HD-PROST was  
 284 assessed on several data sets (not reported here) by comparing the quality of the  
 285 reconstructions with several regularization parameters  $\lambda$  (the same  $\lambda$  was used for all  
 286 patches:  $\lambda_p = \lambda$  for all  $p$ ). The optimal value was shown to be proportional to the number  
 287 of MRF measurements and was set to  $\lambda = -1e^{-3} \times n + 0.4$  for each decomposition, with

288  $n$  being the number of MRF radial spokes. The joint MR reconstruction and denoising steps  
 289 were iteratively interleaved and the reconstruction was terminated after five ADMM  
 290 iterations. All parameters were empirically optimized on one dataset by visual inspection  
 291 and the same values were used for all other subjects.

292 The proposed HD-PROST reconstruction for 2D MRF was compared to the low-rank  
 293 inversion (LRI) reconstruction (24,38) with  $r = 10$  and using 10 conjugate gradient  
 294 iterations, which were seen to be enough for convergence.

295

### 296 *Dictionary generation and pattern recognition*

297 The MRF dictionary was generated using the Extended Phase Graphs (EPG) formalism  
 298 (47). The dictionary was calculated for a  $T_1$  in the range of  
 299 ([50: 10: 1400, 1430: 30: 1600, 1700: 100: 2200, 2400: 200: 3000] ms) and  $T_2$  in the  
 300 range of ([5: 2: 80, 85: 5: 150, 160: 10: 300, 330: 30: 600] ms). Slice profile was  
 301 simulated for each RF pulse using 51 isochromats distributed along the slice selection  
 302 direction and was included in the dictionary generation to correct for profile imperfections  
 303 (48). Template matching between fingerprints and dictionary were performed using the  
 304 inner product as in (1).

## 305 **Accelerated 3D Multi-Contrast Magnetization Transfer Imaging**

### 306 *Acquisition*

307 A 3D accelerated MTC experiment was performed to evaluate the proposed HD-PROST  
 308 reconstruction on 3D Cartesian acquisitions with multiple MT-weighted images. In vivo  
 309 brain acquisitions were performed on three healthy subjects (one man, age range: 24-30  
 310 years) on a 1.5T MR scanner (Magnetom Aera, Siemens Healthcare, Erlangen, Germany)  
 311 equipped with a 20-channel head coil. Acquisitions consisted of one reference image  
 312 without magnetization preparation, and five images with different MT preparations (i.e. in  
 313 this study,  $L = 6$  and  $M_z > 1$ ).

314 A prototype 3D Cartesian variable-density trajectory was integrated in the sequence to  
 315 allow for fast acquisition of multiple MT-weighted images. The Cartesian trajectory with  
 316 spiral profile order (33,49) samples the  $k_y$ - $k_z$  phase-encoding plane following approximate  
 317 spiral interleaves on the Cartesian grid with variable density along each spiral arm and with  
 318 two successive spiral interleaves being rotated by the golden ratio. A golden angle rotation  
 319 between different contrast acquisitions was incorporated here (shifted VD-CASPR) to  
 320 introduce incoherently distributed aliasing artifacts along the contrast dimension and noise-  
 321 like artifacts in the spatial dimension, which is beneficial from a CS and low-rank point of  
 322 view (50).

323 The MT weighting was achieved by applying a train of sinc-shaped, off-resonance RF  
 324 pulses before image acquisition with the following parameters: MT off-resonance  
 325 frequency ( $\Delta F$ ) = 3 kHz, 20 MT pulse repetitions, MT bandwidth = 401 Hz/pixel. Relevant  
 326 scan parameters included: 3D gradient echo sequence, axial orientation, FOV =  
 327 230x230x160 mm<sup>3</sup>, nominal resolution 1x1x2 mm<sup>3</sup>, FA = 15°, TE = 1.78 ms, TR = 4.06  
 328 ms, receiver bandwidth = 925 Hz/pixel, 32 readouts per spiral interleave. Six measurements  
 329 were acquired with different MT pulse flip angles ( $\alpha_{MT} =$   
 330  $[0^\circ, 160^\circ, 320^\circ, 480^\circ, 640^\circ, 800^\circ]$ ) with five seconds pause between them. Acquisitions  
 331 were performed with an acceleration factor of 6.5-fold for each weighted image. The total  
 332 scan time to acquire the six measurements was 13:18 [min:sec]. A fully-sampled acquisition  
 333 of the six measurements at this resolution would take more than one hour. Therefore, for  
 334 comparison purposes, an additional fully-sampled acquisition was performed only for the  
 335 reference image ( $\alpha_{MT} = 0^\circ$ ). The total scan time for this single-contrast fully-sampled  
 336 acquisition was 12:57 [min:sec].

### 337 ***Reconstruction***

338 The following parameters were used for the 3D multi-MT reconstruction: patch size  $N =$   
 339  $7 \times 7 \times 7$ , search window =  $20 \times 20 \times 20$ , number of similar 3D patches selected  $K = 30$ ,  
 340 patch offset = 3, ADMM iterations = 5,  $CG_{eps} = 1e^{-7}$ ,  $CG_{iter} = 10$ . The threshold  
 341 parameters  $\lambda$  and  $\mu$  were empirically set to 0.1 and  $5e^{-3}$ , respectively. Coil sensitivity maps

342 were estimated from the fully-sampled k-space center using the eigenvalue-based approach  
343 ESPIRiT.

344 The proposed HD-PROST reconstruction was compared with two well-established state-  
345 of-the-art reconstruction techniques. The first technique is LLR, proposed by T. Zhang (26)  
346 for accelerating MR parameter mapping. LLR exploits the redundancy in the contrast  
347 dimension on local image regions in an iterative low-rank framework. LLR was  
348 implemented using our ADMM framework by replacing the patch-based denoising step by  
349 the low-rank thresholding. This allows for fair comparisons since the same optimization  
350 was used and only the manner in which the denoising is performed was modified. The rank  
351 threshold  $\lambda_{LLR}$  was fixed and set to 5% of the highest singular value. Since the acquired  
352 MT-weighted data was fully-sampled in the read-out direction, the MR reconstruction step  
353 was accelerated for both LLR and HD-PROST reconstructions by computing a one-  
354 dimensional inverse FFT and considering multiple separable 2D reconstruction problems  
355 independently.

356 The second technique is an iterative CS reconstruction with spatial Wavelet sparsity  
357 constraint as described in (12) and implemented in the BART toolbox (51). CS  
358 reconstruction was performed for each contrast independently. The regularization  
359 parameter  $\lambda_{CS}$  was optimized experimentally and set to 0.01. Visual assessment was  
360 performed between the different techniques and the fully-sampled acquisition.

361

## 362 **Results**

### 363 **Accelerated 2D Magnetic Resonance Fingerprinting**

#### 364 *Phantom study*

365 Figure 2 shows  $T_1$  and  $T_2$  values for the 2D MRF phantom experiments with 2000, 1000  
366 and 500 time-points in comparison to the gold standard IRSE and SE acquisitions for both  
367 LRI and HD-PROST reconstructions.  $T_1$  values obtained from both strategies were in good



368 agreement with the IRSE acquisition even for reconstructions with 500 time-points, with  
369 an excellent linear relationship with the reference  $T_1$  values (goodness-to-fit  $R^2 > 0.98$ ).  
370  $T_2$  accuracy was also preserved with the proposed reconstruction with a slight  $T_2$   
371 degradation observed for long  $T_2$  values and high acceleration for both reconstructions.  
372 Figure 3 depicts the precision of  $T_1$  and  $T_2$  values, as characterized by the standard deviation  
373 (aggregated based on the variance of each vial). An increase in precision was observed for  
374 both  $T_1/T_2$  values using the proposed HD-PROST reconstruction compared with LRI even  
375 for reconstructions with 500 time-points, corresponding to 2.5s scan time. Corresponding  
376  $T_1$  and  $T_2$  maps are shown in Supporting Information Figure S2. From the above analysis,  
377 it follows that 500 MRF time-points or less might be sufficient and suitable for accurate  
378 and precise in vivo  $T_1/T_2$  maps acquisitions in less than 2.5 seconds.

### 379 *In vivo study*

380 Figure 4 depicts the first four 2D MRF singular images from the reference LRI and the  
381 proposed HD-PROST reconstruction for one representative subject reconstructed with  
382 1000 time-points. A clear superior image quality can be observed on the HD-PROST  
383 singular images with a sharp and clear delineation of the brain structures. A high level of  
384 streaking artifacts and noise can be seen on the last singular value components (e.g. singular  
385 images #3 and #4) with LRI, whereas HD-PROST not only produces images with  
386 considerably less noise but is also able to recover small structures that were lost below the  
387 noise level with LRI (Figure 4, yellow arrows).  $T_1$  and  $T_2$  maps are displayed in Figure 5  
388 and Figure 6 for two subjects and three different measurement lengths (2000, 1000 and 500  
389 time-points) for both LRI and HD-PROST reconstructions.

390 The reconstructed maps from one additional subject are shown in Supporting Information  
391 Figure S3. A number of interesting observations can be made. Reducing the number of  
392 measurements tends to blur the  $T_1$  maps with LRI while the  $T_2$  maps suffer from noise  
393 amplification, showing an overall noisier appearance. Conversely, by enforcing low-rank  
394 in the local, non-local and contrast dimension, HD-PROST reconstruction delivers higher  
395 image quality, recovering sharpness for  $T_1$  and reducing the noise for  $T_2$ . The improvement

396 is more pronounced for the 500 time-points acquisition (2.5s scan time). In vivo  $T_1$  and  $T_2$   
397 relaxation times measured in regions of interest in the white and grey matters with LRI and  
398 the proposed HD-PROST are shown in Table 1. Both reconstructions converged to very  
399 comparable values that are in good agreement with values obtained from the literature for  
400  $T_1$ . Moreover, the proposed HD-PROST reconstruction tends to lower the standard  
401 deviations of  $T_1$  and  $T_2$  times, which is in accordance with the noise reduction seen in the  
402 quantitative maps. Note that the  $T_2$  relaxation times for both techniques are slightly biased  
403 and depart from the literature values. This may be partly explained by the fact that  $B_1$   
404 imperfections (52) as well as other sources of bias such as magnetization transfer (53) and  
405 diffusion-weighting (54) were not considered in the proposed study. The average  
406 reconstruction time for 2D MRF with HD-PROST was about 10 minutes per data set.  
407 Additional comparisons with single-contrast PROST reconstruction (i.e. reconstructing  
408 each singular image independently) and with a global low-rank tensor decomposition (in  
409 the spirit of cardiac multitasking (28,29)) are provided in Supporting Information Figure  
410 S4.

411

### 412 **Accelerated 3D Multi-Contrast Magnetization Transfer Imaging**

413 Figure 7 depicts four axial slices obtained with HD-PROST reconstruction of the 6.5-fold  
414 undersampled 3D MT-weighted images in a representative subject in comparison to the  
415 fully-sampled acquisition. Only the reference image obtained with  $\alpha_{MT} = 0^\circ$ , is shown  
416 here. Similar image quality is observed between the 6.5-fold accelerated HD-PROST  
417 approach and the fully-sampled scan. Line profiles going through a structure with sharp  
418 edges are shown in Figure 7c, showing excellent agreement between HD-PROST and the  
419 fully-sampled reference. Six different undersampled MT-weighted images were acquired  
420 in 13min 18s, whereas the fully-sampled acquisition of a single contrast took 12min 57s.  
421 Figure 8 compares HD-PROST to conventional CS reconstruction from a 6.5-fold  
422 acceleration. Comparisons with zero-filling and LLR reconstructions are provided in  
423 Supporting Information Figures S5 and S6. As expected, zero-filling exhibits a low image

424 quality with apparent aliasing artifacts and blurring. Exploiting contrast redundancy  
425 through local image regions with LLR improves the overall image quality and enables the  
426 recovery of small structures, particularly for low-contrast images (e.g.  $\alpha_{MT} = 800^\circ$ ), while  
427 the apparent noise is still large. By contrast, CS reconstruction with spatial regularization  
428 is able to recover images with reduced level of noise but fails to recover small structures  
429 for low contrast images (see Figure 8, red arrows). Enforcing multi-dimensional low-rank  
430 and capturing 3D information of local and non-local 3D patches through the multiple MT-  
431 weighted images with HD-PROST allows to recover small structures and reduced the level  
432 of apparent noise, resulting in high image quality for all different contrasts. Reconstructions  
433 from two other subjects can be seen in Supporting Information Figures S7 and S8. The  
434 average computation time for 3D HD-PROST reconstruction was about 27 minutes for all  
435 6 contrasts in the acquisitions performed in this study.

436

## 437 **Discussion**

438 HD-PROST reconstruction enables accelerated acquisition of 2D or 3D multi-contrast MR  
439 images by exploiting the high local and non-local redundancies, and the similarities  
440 between the multi-contrast images through a high-order low-rank tensor approximation.

441 The proposed technique was applied to accelerated non-Cartesian 2D MRF and accelerated  
442 Cartesian 3D MTC imaging to enable undersampling factors that go beyond the limit of  
443 traditional PI and CS reconstructions (i.e. about 2.5 seconds acquisition for 2D MRF, and  
444 6.5-fold acceleration for 3D MTC), while removing residual aliasing artifacts. Phantom  
445 experiments in accelerated 2D MRF were carried out to investigate the impact of rapid  
446 acquisition (i.e. reduced number of time-point images) on accuracy and precision of  $T_1$  and  
447  $T_2$  relaxation times. High agreement with reference  $T_1/T_2$  values was observed using HD-  
448 PROST, even for high accelerations, with increased precision compared to conventional  
449 LRI reconstruction.

450 For in vivo MRF, streaking artifacts and noise amplification often propagated in the  $T_1$   
451 maps with LRI reconstruction, while blurring was observed on the  $T_2$  maps for high  
452 acceleration factors. HD-PROST achieved improved sharpness and reduced noise level in  
453 comparison to the low-rank inversion reconstruction, especially for acquisitions with  
454 reduced number of time-points. Nevertheless, a systemic underestimation of the  $T_2$  values,  
455 previously reported in MRF literature, was observed in the in vivo study. This finding may  
456 be partly explained by the fact that  $B_1$  imperfections (52), magnetization transfer (53), and  
457 diffusion-weighting (54) were not considered in this MRF study and could lead to  
458 inaccurate  $T_2$  measurements.

459 HD-PROST has a modular design, which allows for its straightforward extension to 3D or  
460 n-D imaging by simple patch vectorization. In line with the previous 2D MRF study,  
461 accelerated 3D MTC using HD-PROST showed improved image quality over conventional  
462 CS and low-rank reconstructions for an acceleration factor of 6.5, with visual quality  
463 comparable to the fully-sampled acquisition. High denoising performance was achieved  
464 due to the existence of multiple MT-weighted images of the same object with varying  
465 contrasts, leading to high redundancy which can be exploited by HD-PROST. The pseudo-  
466 random sampling, given by the proposed shifted VD-CASPR, causes aliasing artifacts that  
467 spread incoherently in the contrast dimension and exhibits noise-like perturbations at the  
468 image scale, providing an excellent basis for HD-PROST reconstruction. This study was  
469 only performed on a small number of subjects and further evaluations on larger cohorts are  
470 needed. Nevertheless, this proof of concept suggests an opportunity for high-resolution  
471 quantitative magnetization transfer imaging in a clinically feasible scan time.

472 The efficient multithreaded implementation of the high-order patch-based denoising  
473 allowed for fast image denoising of large data sets (e.g. in the order of 200 seconds for a  
474 3D data set with a matrix size of  $200 \times 256 \times 104 \times 6$ ). Further speedups could be  
475 achieved to reach clinically acceptable runtimes by implementing the joint MR  
476 optimization step on multiple GPUs (55) and using coil compression algorithms (56).

477 HD-PROST imposes low-rank in the complex domain, and therefore captures the possible  
478 cross-correlation observed between the real and imaginary components, allowing for  
479 accurate and faithful reconstruction of both phase and magnitude. Our framework makes  
480 use of ADMM to decouple the main optimization problem into two simpler sub-problems  
481 that have straightforward solutions. Although most of the noise and undersampling artifacts  
482 can be efficiently removed after the first iteration, aliasing may still exist depending on the  
483 quality of the input images. This behavior mainly stems from the fact that corrupted images  
484 can negatively affect the block matching step, resulting in a sub-optimal grouping. Thus,  
485 several ADMM iterations (five in this study) are needed to achieve good image quality  
486 reconstructions.

487 The technique proposed in this paper can potentially change conventional multi-contrast  
488 imaging by making efficient use of the rich and redundant information available locally and  
489 temporally. Two applications were introduced in this study, nonetheless HD-PROST stays  
490 generic and should be easily extendable to many MR applications where multiple contrasts  
491 are involved, such as conventional  $T_1$  and  $T_2$  mapping, perfusion imaging (57), 4D flow  
492 MRI (58) or low SNR applications such as arterial spin labeling (59).

## 493 **Conclusion**

494 We present a new framework, termed HD-PROST, for efficient reconstruction of  
495 undersampled multi-channel multi-contrast MR images. HD-PROST aims at achieving  
496 high image quality by exploiting the high local and non-local redundancies, and the  
497 similarities between the multi-contrast images through a high-dimensionality low-rank  
498 tensor decomposition. HD-PROST was validated in accelerated 2D MRF to generate  
499 precise  $T_1$  and  $T_2$  maps in about 2.5 seconds without affecting  $T_1/T_2$  accuracy. For  
500 accelerated multiple 3D MT-weighted acquisitions, HD-PROST can recover high quality  
501 images, comparable to a fully-sampled acquisition, in a clinically reasonable timeframe.  
502 The straightforward, yet efficient, application of HD-PROST to 2D and 3D multi-contrast  
503 data sets, provides several opportunities for future research, particularly in areas where  
504 high-dimensionality is likely to increase in importance.

## 505 **Acknowledgement**

506 The authors would like to thank Dr. Radhouene Neji (Siemens Healthcare, Frimley, United  
507 Kingdom) and Dr. Torben Schneider (Philips Healthcare, United Kingdom) for their  
508 assistance in the implementation of the MR sequences presented in this study. The authors  
509 acknowledge financial support from: (1) EPSRC EP/P001009/, EP/P032311/1, EPSRC  
510 EP/P007619, (2) Wellcome EPSRC Centre for Medical Engineering (NS/ A000049/1), and  
511 (3) the Department of Health via the National Institute for Health Research (NIHR)  
512 comprehensive Biomedical Research Centre award to Guy's & St Thomas' NHS  
513 Foundation Trust in partnership with King's College London and King's College Hospital  
514 NHS Foundation Trust. The views expressed are those of the authors and not necessarily  
515 those of the NHS, the NIHR or the Department of Health.

516

517 **References**

- 518 1. Ma D, Gulani V, Seiberlich N, Liu K, Sunshine JL, Duerk JL, Griswold MA.  
519 Magnetic resonance fingerprinting. *Nature* [Internet] 2013;495:187–92. doi:  
520 10.1038/nature11971.
- 521 2. Jiang Y, Ma D, Seiberlich N, Gulani V, Griswold MA. MR fingerprinting using  
522 fast imaging with steady state precession (FISP) with spiral readout. *Magn. Reson.*  
523 *Med.* 2015;74:1621–1631. doi: 10.1002/mrm.25559.
- 524 3. Xue H, Shah S, Greiser A, Guetter C, Littmann A, Jolly M-P, Arai AE, Zuehlsdorff  
525 S, Guehring J, Kellman P. Motion correction for myocardial T1 mapping using  
526 image registration with synthetic image estimation. *Magn. Reson. Med.* [Internet]  
527 2012;67:1644–1655. doi: 10.1002/mrm.23153.
- 528 4. Roujol S, Basha TA, Weingärtner S, Akçakaya M, Berg S, Manning WJ, Nezafat  
529 R. Impact of motion correction on reproducibility and spatial variability of  
530 quantitative myocardial T2mapping. *J. Cardiovasc. Magn. Reson.* 2015;17. doi:  
531 10.1186/s12968-015-0141-1.
- 532 5. Cruz G, Jaubert O, Schneider T, Botnar RM, Prieto C. Rigid Motion Corrected  
533 Magnetic Resonance Fingerprinting. *Magn. Reson. Med.* 2019;81:947–961. doi:  
534 <https://doi.org/10.1002/mrm.27448>.
- 535 6. Mehta BB, Ma D, Pierre EY, Jiang Y, Coppo S, Griswold MA. Image  
536 reconstruction algorithm for motion insensitive MR Fingerprinting (MRF): MORF.  
537 *Magn. Reson. Med.* 2018:1–16. doi: 10.1002/mrm.27227.
- 538 7. Pruessmann KP, Weiger M, Scheidegger MB, Boesiger P. SENSE: sensitivity  
539 encoding for fast MRI. *Magn. Reson. Med.* [Internet] 1999;42:952–62. doi:  
540 10.1002/(SICI)1522-2594(199911)42:5<952::AID-MRM16>3.0.CO;2-S.
- 541 8. Griswold M a, Jakob PM, Heidemann RM, Nittka M, Jellus V, Wang J, Kiefer B,  
542 Haase A. Generalized autocalibrating partially parallel acquisitions (GRAPPA).  
543 *Magn. Reson. Med.* [Internet] 2002;47:1202–10. doi: 10.1002/mrm.10171.

- 544 9. Lustig M, Pauly JM. SPIRiT: Iterative self-consistent parallel imaging  
545 reconstruction from arbitrary k-space. *Magn. Reson. Med.* [Internet] 2010;64:457–  
546 71. doi: 10.1002/mrm.22428.
- 547 10. Bilgic B, Kim TH, Liao C, Manhard MK, Wald LL, Haldar JP, Setsompop K.  
548 Improving parallel imaging by jointly reconstructing multi-contrast data. *Magn.*  
549 *Reson. Med.* 2018;80:619–632. doi: 10.1002/mrm.27076.
- 550 11. Li Y, Dumoulin C. Correlation imaging for multiscan MRI with parallel data  
551 acquisition. *Magn. Reson. Med.* 2012;68:2005–2017. doi: 10.1002/mrm.24206.
- 552 12. Lustig M, Donoho D, Pauly JM. Sparse MRI: The application of compressed  
553 sensing for rapid MR imaging. *Magn. Reson. Med.* [Internet] 2007;58:1182–95. doi:  
554 10.1002/mrm.21391.
- 555 13. Doneva M, Börnert P, Eggers H, Stehning C, Sénégas J, Mertins A. Compressed  
556 sensing reconstruction for magnetic resonance parameter mapping. *Magn. Reson.*  
557 *Med.* [Internet] 2010;64:1114–20. doi: 10.1002/mrm.22483.
- 558 14. Velikina J V., Alexander AL, Samsonov A. Accelerating MR parameter mapping  
559 using sparsity-promoting regularization in parametric dimension. *Magn. Reson.*  
560 *Med.* 2013;70:1263–1273. doi: 10.1002/mrm.24577.
- 561 15. Gong E, Huang F, Ying K, Wu W, Wang S, Yuan C. PROMISE: Parallel-  
562 imaging and compressed-sensing reconstruction of multicontrast imaging using  
563 Sharable information. *Magn. Reson. Med.* [Internet] 2014;73:523–535. doi:  
564 10.1002/mrm.25142.
- 565 16. Bilgic B, Goyal VK, Adalsteinsson E. Multi-contrast reconstruction with  
566 Bayesian compressed sensing. *Magn. Reson. Med.* [Internet] 2011;66:1601–15. doi:  
567 10.1002/mrm.22956.
- 568 17. Zhang L, Athavale P, Pop M, Wright GA. Multicontrast reconstruction using  
569 compressed sensing with low rank and spatially varying edge-preserving constraints  
570 for high-resolution MR characterization of myocardial infarction. *Magn. Reson.*



- 571 Med. 2017;78:598–610. doi: 10.1002/mrm.26402.
- 572 18. Huang J, Chen C, Axel L. Fast multi-contrast MRI reconstruction. *Magn. Reson.*  
573 *Imaging [Internet]* 2014;32:1344–1352. doi: 10.1016/j.mri.2014.08.025.
- 574 19. Ehrhardt MJ, Betcke MM. Multi-Contrast MRI Reconstruction with Structure-  
575 Guided Total Variation. *SIAM J. Imaging Sci. [Internet]* 2016;9:1084–1106. doi:  
576 10.1137/15M1047325.
- 577 20. Majumdar A, Ward RK. Joint reconstruction of multiecho MR images using  
578 correlated sparsity. *Magn. Reson. Imaging [Internet]* 2011;29:899–906. doi:  
579 10.1016/j.mri.2011.03.008.
- 580 21. Knoll F, Holler M, Koesters T, Otazo R, Bredies K, Sodickson DK. Joint MR-  
581 PET Reconstruction Using a Multi-Channel Image Regularizer. *IEEE Trans. Med.*  
582 *Imaging* 2017;36:1–16. doi: 10.1109/TMI.2016.2564989.
- 583 22. Peng X, Ying L, Liu Y, Yuan J, Liu X, Liang D. Accelerated exponential  
584 parameterization of T2 relaxation with model-driven low rank and sparsity priors  
585 (MORASA). *Magn. Reson. Med.* 2016;76:1865–1878. doi: 10.1002/mrm.26083.
- 586 23. Tamir JI, Uecker M, Chen W, Lai P, Alley MT, Vasanawala SS, Lustig M. T2  
587 shuffling: Sharp, multicontrast, volumetric fast spin-echo imaging. *Magn. Reson.*  
588 *Med.* 2017;77:180–195. doi: 10.1002/mrm.26102.
- 589 24. Zhao B, Lu W, Hitchens TK, Lam F, Ho C, Liang ZP. Accelerated MR parameter  
590 mapping with low-rank and sparsity constraints. *Magn. Reson. Med.* 2015;74:489–  
591 498. doi: 10.1002/mrm.25421.
- 592 25. Trzasko J, Manduca A. Local versus Global Low-Rank Promotion in Dynamic  
593 MRI Series Reconstruction. *Proc Intl Soc Mag Reson Med* 2011;24:4371.
- 594 26. Zhang T, Pauly JM, Levesque IR. Accelerating parameter mapping with a locally  
595 low rank constraint. *Magn. Reson. Med.* 2015;73:655–661. doi:  
596 10.1002/mrm.25161.
- 597 27. Zhang T, Cheng JY, Potnick AG, Barth RA, Alley MT, Uecker M, Lustig M,

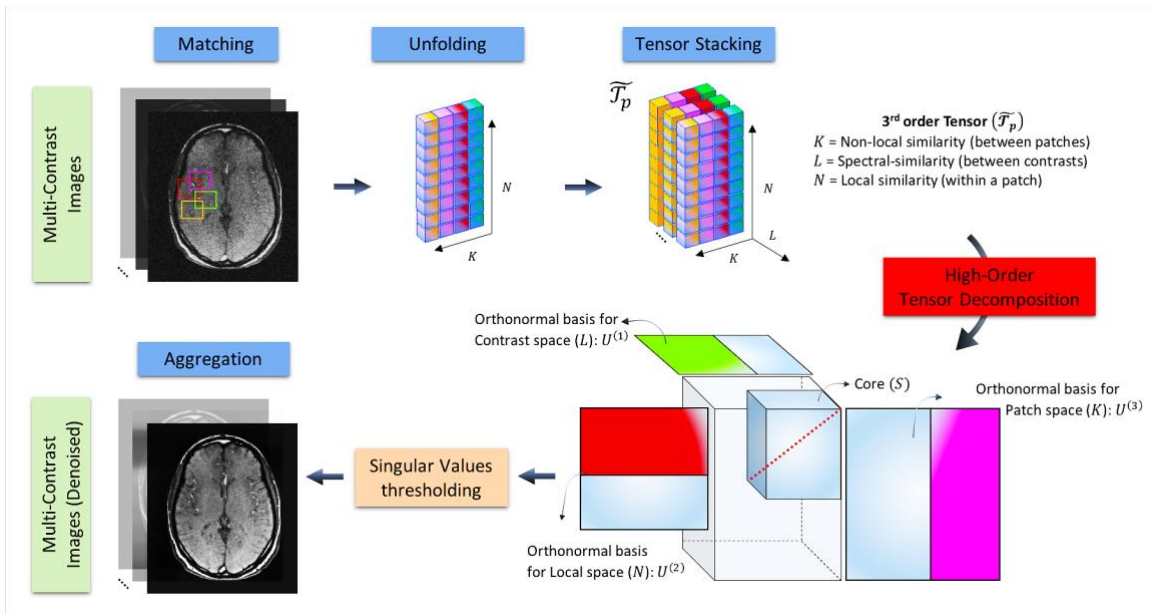
- 598 Pauly JM, Vasanawala SS. Fast pediatric 3D free-breathing abdominal dynamic  
599 contrast enhanced MRI with high spatiotemporal resolution. *J. Magn. Reson.*  
600 *Imaging* 2015. doi: 10.1002/jmri.24551.
- 601 28. Christodoulou AG, Shaw JL, Nguyen C, Yang Q, Xie Y, Wang N, Li D. Magnetic  
602 resonance multitasking for motion-resolved quantitative cardiovascular imaging.  
603 *Nat. Biomed. Eng.* [Internet] 2018;2:215–226. doi: 10.1038/s41551-018-0217-y.
- 604 29. Shaw JL, Yang Q, Zhou Z, Deng Z, Nguyen C, Li D, Christodoulou AG. Free-  
605 breathing, non-ECG, continuous myocardial  $T_1$  mapping with cardiovascular  
606 magnetic resonance Multitasking. *Magn. Reson. Med.* [Internet] 2018:1–14. doi:  
607 10.1002/mrm.27574.
- 608 30. Akçakaya M, Basha TA, Chan RH, Manning WJ, Nezafat R. Accelerated  
609 isotropic sub-millimeter whole-heart coronary MRI: Compressed sensing versus  
610 parallel imaging. *Magn. Reson. Med.* 2014;71:815–822. doi: 10.1002/mrm.24683.
- 611 31. Bustin A, Voilliot D, Menini A, Felblinger J, de Chillou C, Burschka D,  
612 Bonnemains L, Odille F. Isotropic Reconstruction of MR Images using 3D Patch-  
613 Based Self-Similarity Learning. *IEEE Trans. Med. Imaging* 2018;37:1932–1942.  
614 doi: 10.1109/TMI.2018.2807451.
- 615 32. Akçakaya M, Basha TA, Goddu B, Goepfert LA, Kissinger K V., Tarokh V,  
616 Manning WJ, Nezafat R. Low-dimensional-structure self-learning and thresholding:  
617 Regularization beyond compressed sensing for MRI Reconstruction. *Magn. Reson.*  
618 *Med.* 2011;66:756–767. doi: 10.1002/mrm.22841.
- 619 33. Bustin A, Ginami G, Cruz G, Correia T, Ismail TF, Rashid I, Neji R, Botnar RM,  
620 Prieto C. Five-minute whole-heart coronary MRA with sub-millimeter isotropic  
621 resolution, 100% respiratory scan efficiency, and 3D-PROST reconstruction. *Magn.*  
622 *Reson. Med.* [Internet] 2018;00:1–14. doi: 10.1002/mrm.27354.
- 623 34. Boyd S, Parikh N, Chu E, Peleato B, Eckstein J. Distributed Optimization and  
624 Statistical Learning via the Alternating Direction Method of Multipliers. *Found.*

- 625 Trends Mach. Learn. [Internet] 2011;3:1–122. doi: 10.1561/22000000016.
- 626 35. Hestenes MR, Stiefel E. Methods of conjugate gradients for solving linear  
627 systems. J. Res. Natl. Bur. Stand. (1934). [Internet] 1952;49:409. doi:  
628 10.6028/jres.049.044.
- 629 36. De Lathauwer L, De Moor B, Vandewalle J. A multilinear singular value  
630 decomposition. SIAM J. Matrix Anal. Appl. 2000. doi:  
631 10.1137/S0895479896305696.
- 632 37. Tucker LR. Some mathematical notes on three-mode factor analysis.  
633 Psychometrika 1966. doi: 10.1007/BF02289464.
- 634 38. Zhao B, Setsompop K, Adalsteinsson E, Gagoski B, Ye H, Ma D, Jiang Y, Ellen  
635 Grant P, Griswold MA, Wald LL. Improved magnetic resonance fingerprinting  
636 reconstruction with low-rank and subspace modeling. Magn. Reson. Med.  
637 2018;79:933–942. doi: 10.1002/mrm.26701.
- 638 39. Assländer J, Cloos MA, Knoll F, Sodickson DK, Hennig J, Lattanzi R. Low rank  
639 alternating direction method of multipliers reconstruction for MR fingerprinting.  
640 Magn. Reson. Med. 2018;79:83–96. doi: 10.1002/mrm.26639.
- 641 40. Tang S, Fernandez-Granda C, Lannuzel S, Bernstein B, Lattanzi R, Cloos M,  
642 Knoll F, Assländer J. Multicompartment Magnetic Resonance Fingerprinting. arXiv  
643 Prepr. arXiv1802.10492 [Internet] 2018.
- 644 41. Doneva M, Amthor T, Koken P, Sommer K, Börnert P. Matrix completion-based  
645 reconstruction for undersampled magnetic resonance fingerprinting data. Magn.  
646 Reson. Imaging [Internet] 2017;41:41–52. doi: 10.1016/j.mri.2017.02.007.
- 647 42. Cline CC, Chen X, Mailhe B, Wang Q, Pfeuffer J, Nittka M, Griswold MA,  
648 Speier P, Nadar MS. AIR-MRF: Accelerated iterative reconstruction for magnetic  
649 resonance fingerprinting. Magn. Reson. Imaging [Internet] 2017;41:29–40. doi:  
650 10.1016/j.mri.2017.07.007.
- 651 43. Captur G, Gatehouse P, Keenan KE, et al. A medical device-grade T1 and ECV

- 652 phantom for global T1 mapping quality assurance - the T1 Mapping and ECV  
653 Standardization in cardiovascular magnetic resonance (TIMES) program. *J.*  
654 *Cardiovasc. Magn. Reson.* [Internet] 2016;18:1–20. doi: 10.1186/s12968-016-0280-  
655 z.
- 656 44. Assländer J, Lattanzi R, Sodickson DK, Cloos MA. Relaxation in Spherical  
657 Coordinates: Analysis and Optimization of pseudo-SSFP based MR-Fingerprinting.  
658 arXiv Prepr. arXiv1703.00481. [Internet] 2017:1–22. doi:  
659 10.1017/CBO9781107415324.004.
- 660 45. Uecker M, Lai P, Murphy MJ, Virtue P, Elad M, Pauly JM, Vasanawala SS,  
661 Lustig M. ESPIRiT-an eigenvalue approach to autocalibrating parallel MRI: Where  
662 SENSE meets GRAPPA. *Magn. Reson. Med.* [Internet] 2013;194:990–1001. doi:  
663 10.1002/mrm.24751.
- 664 46. Greengard L, Lee J-Y. Accelerating the Nonuniform Fast Fourier Transform.  
665 *SIAM Rev.* [Internet] 2004;46:443–454. doi: 10.1137/S003614450343200X.
- 666 47. Weigel M. Extended phase graphs: Dephasing, RF pulses, and echoes - Pure and  
667 simple. *J. Magn. Reson. Imaging* 2015;41:266–295. doi: 10.1002/jmri.24619.
- 668 48. Ma D, Coppo S, Chen Y, McGivney DF, Jiang Y, Pahwa S, Gulani V, Griswold  
669 MA. Slice profile and B1 corrections in 2D magnetic resonance fingerprinting.  
670 *Magn. Reson. Med.* 2017;78:1781–1789. doi: 10.1002/mrm.26580.
- 671 49. Prieto C, Doneva M, Usman M, Henningsson M, Greil G, Schaeffter T, Botnar  
672 RM. Highly efficient respiratory motion compensated free-breathing coronary mra  
673 using golden-step Cartesian acquisition. *J. Magn. Reson. Imaging* [Internet]  
674 2015;41:738–746. doi: 10.1002/jmri.24602.
- 675 50. Otazo R, Candès E, Sodickson DK. Low-rank plus sparse matrix decomposition  
676 for accelerated dynamic MRI with separation of background and dynamic  
677 components. *Magn. Reson. Med.* 2015;73:1125–1136. doi: 10.1002/mrm.25240.
- 678 51. Tamir JI, Ong F, Cheng JY, Uecker M, Lustig M. Generalized Magnetic

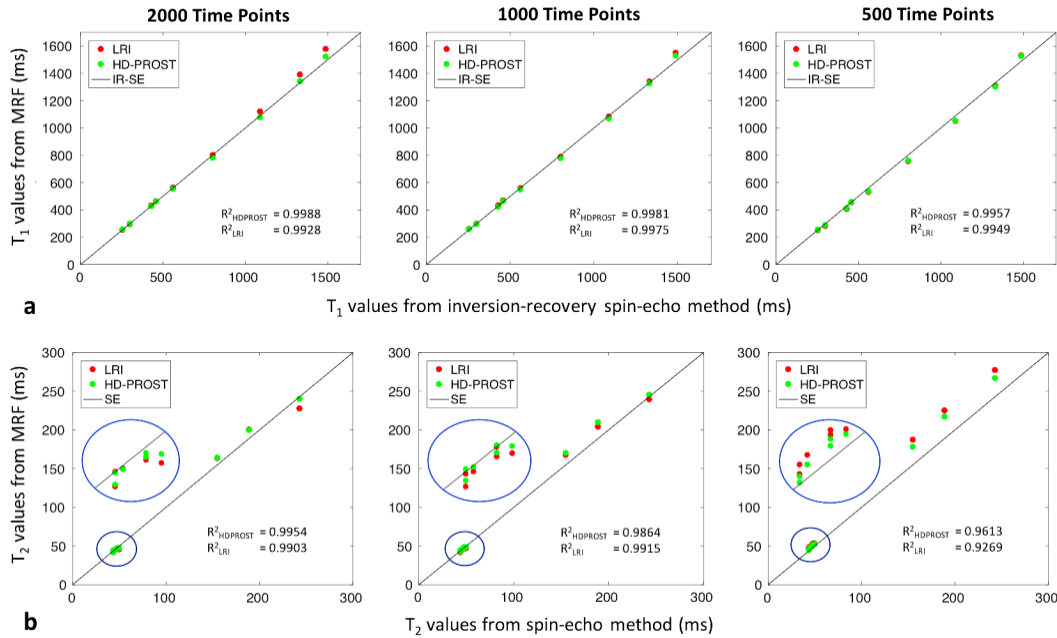
- 679 Resonance Image Reconstruction using The Berkeley Advanced Reconstruction  
680 Toolbox. Proc. ISMRM Work. Data Sampl. Ina. Reconstr. Sedona, AZ [Internet]  
681 2016:33. doi: 10.5281/zenodo.31907.
- 682 52. Buonincontri G, Sawiak SJ. MR fingerprinting with simultaneous B1 estimation.  
683 Magn. Reson. Med. 2016;76:1127–1135. doi: 10.1002/mrm.26009.
- 684 53. Hilbert T, Kober T, Zhao T, Block T, Yu Z, Thiran J-P, Krueger G, Sodickson  
685 D, Cloos M. Mitigating the Effect of Magnetization Transfer in Magnetic Resonance  
686 Fingerprinting. In: Proceedings of the 25th Annual Meeting of ISMRM Hawaii USA.  
687 ; 2018. p. 74.
- 688 54. Kobayashi Y, Tereda Y. Diffusion-weighting caused by spoiler gradients in the  
689 fast imaging with steady-state precession sequence may lead to inaccurate T2  
690 measurements in MR fingerprinting. Magn Reson Med Sci 2018. doi:  
691 <https://doi.org/10.2463/mrms.tn.2018-0027>.
- 692 55. Murphy M, Alley M, Demmel J, Keutzer K, Vasanawala S, Lustig M. Fast  $l_1$ -  
693 SPIRiT compressed sensing parallel imaging MRI: scalable parallel implementation  
694 and clinically feasible runtime. IEEE Trans. Med. Imaging 2012. doi:  
695 10.1109/TMI.2012.2188039.
- 696 56. Zhang T, Pauly JM, Vasanawala SS, Lustig M. Coil compression for accelerated  
697 imaging with Cartesian sampling. Magn. Reson. Med. [Internet] 2013;69:571–82.  
698 doi: 10.1002/mrm.24267.
- 699 57. Otazo R, Kim D, Axel L, Sodickson DK. Combination of compressed sensing  
700 and parallel imaging for highly accelerated first-pass cardiac perfusion MRI. Magn.  
701 Reson. Med. 2010;64:767–776. doi: 10.1002/mrm.22463.
- 702 58. Cheng JY, Zhang T, Alley MT, Uecker M, Lustig M, Pauly JM, Vasanawala SS.  
703 Comprehensive Multi-Dimensional MRI for the Simultaneous Assessment of  
704 Cardiopulmonary Anatomy and Physiology. Sci. Rep. 2017;7:5330. doi:  
705 10.1038/s41598-017-04676-8.

706 59. Detre JA, Leigh JS, Williams DS, Koretsky AP. Perfusion imaging. *Magn.*  
707 *Reson. Med.* 1992. doi: 10.1002/mrm.1910230106.  
708

709 **Figure Captions**

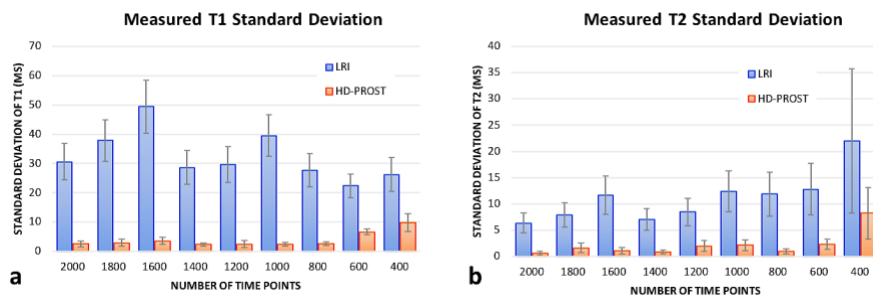
710

711 **Figure 1:** Flowchart of the optimization 2 of the proposed High-Dimensionality Patch-  
 712 based RecOnSTruction (HD-PROST). Denoising of multi-contrast images is performed  
 713 using 2D (respectively 3D) block matching, which groups similar 2D (respectively 3D)  
 714 patches in the multi-contrast images. Similar patches are then unfolded together in a simple  
 715 2D matrix. A third-order tensor  $\mathcal{T}$  is formed by stacking the unfolded patches in the contrast  
 716 dimension. The high-order tensor of size  $N \times K \times L$  admits a low multilinear rank  
 717 approximation and can be compressed, through tensor decomposition, by truncating the  
 718 multilinear singular vectors that correspond to small multilinear singular values. The  
 719 outputs of this step are the denoised multi-contrast images which are then used in the joint  
 720 MR reconstruction process (optimization 1) as prior knowledge. An overview of the  
 721 algorithm is provided in Supporting Information Table S1.



722

723 **Figure 2:** Phantom results for the 2D accelerated MRF using low-rank inversion (LRI) and  
 724 the proposed HD-PROST reconstructions. Plots are comparing the mean  $T_1$  (a) and  $T_2$  (b)  
 725 values derived from 2000, 1000 and 500 time-points, with conventional inversion-recovery  
 726 spin-echo (IRSE) and spin-echo (SE) acquisitions (identity lines).  $T_1$  and  $T_2$  accuracies are  
 727 preserved with the two strategies, with a slight bias observed for long  $T_2$ s at high  
 728 accelerations for both methods. The mean values were obtained from ROIs drawn around  
 729 each phantom vial. Abbreviations – LRI: low-rank inversion, HD-PROST: high-  
 730 dimensionality undersampled patch-based reconstruction.

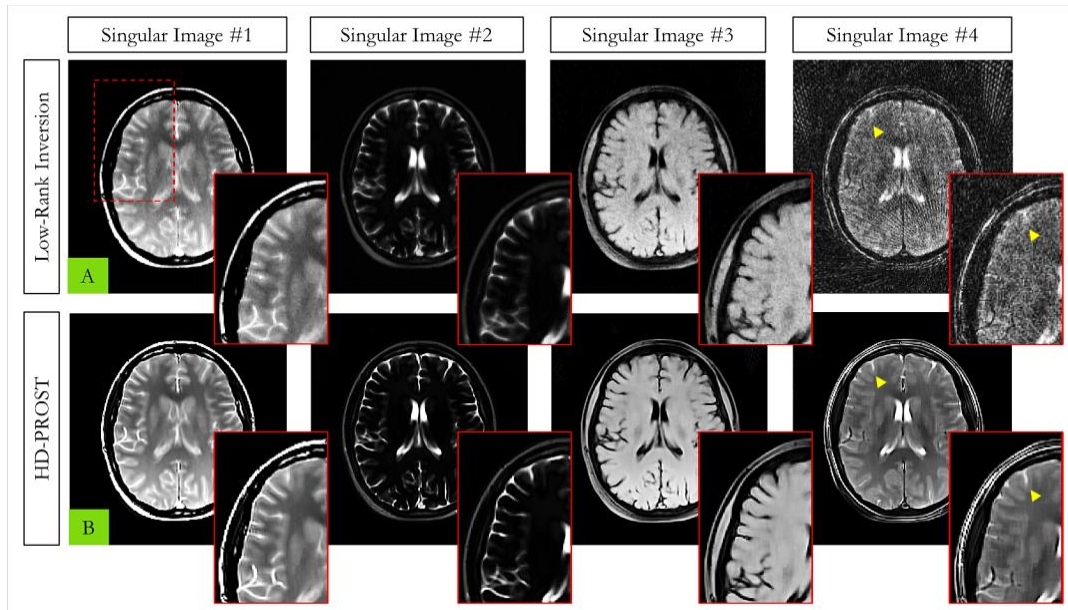


731

732 **Figure 3:** Standard deviations of  $T_1$  (a) and  $T_2$  (b) relaxation times for the phantom study  
 733 are shown for LRI and HD-PROST reconstructions for [400:200:2000] acquired time-point  
 734 images. The precision, as indicated by the standard deviation, was considerably higher with



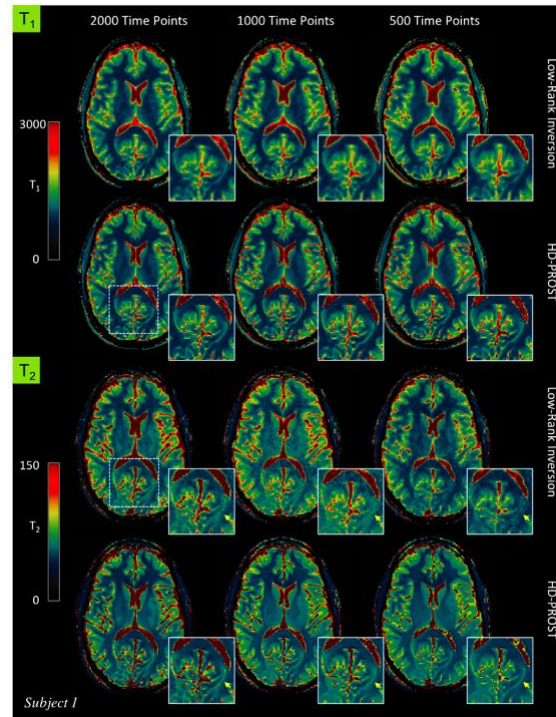
735 the proposed HD-PROST reconstruction, even for shorter acquisitions, while LRI resulted  
 736 in systematic higher standard deviations. The standard deviations were obtained from ROIs  
 737 drawn around each phantom vial. Abbreviations – LRI: low-rank inversion, HD-PROST:  
 738 high-dimensionality undersampled patch-based reconstruction.



739

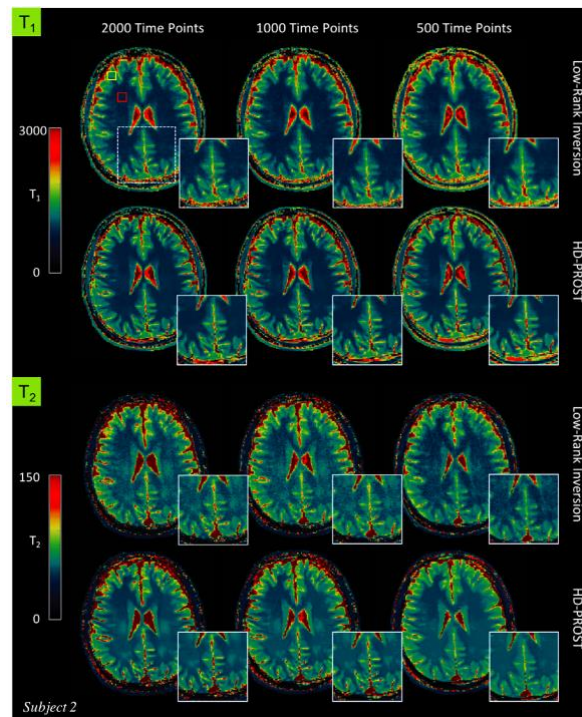
740 **Figure 4:** Reconstructed first four MRF singular images with low-rank inversion (LRI) (a)  
 741 and the proposed HD-PROST (b) in in vivo brain experiments in a representative subject  
 742 acquired with 1000 time-points. A clear improvement in image quality and image sharpness  
 743 can be observed on the HD-PROST reconstruction with considerable reduction of noise and  
 744 streaking artifacts, particularly for the last singular images.

745

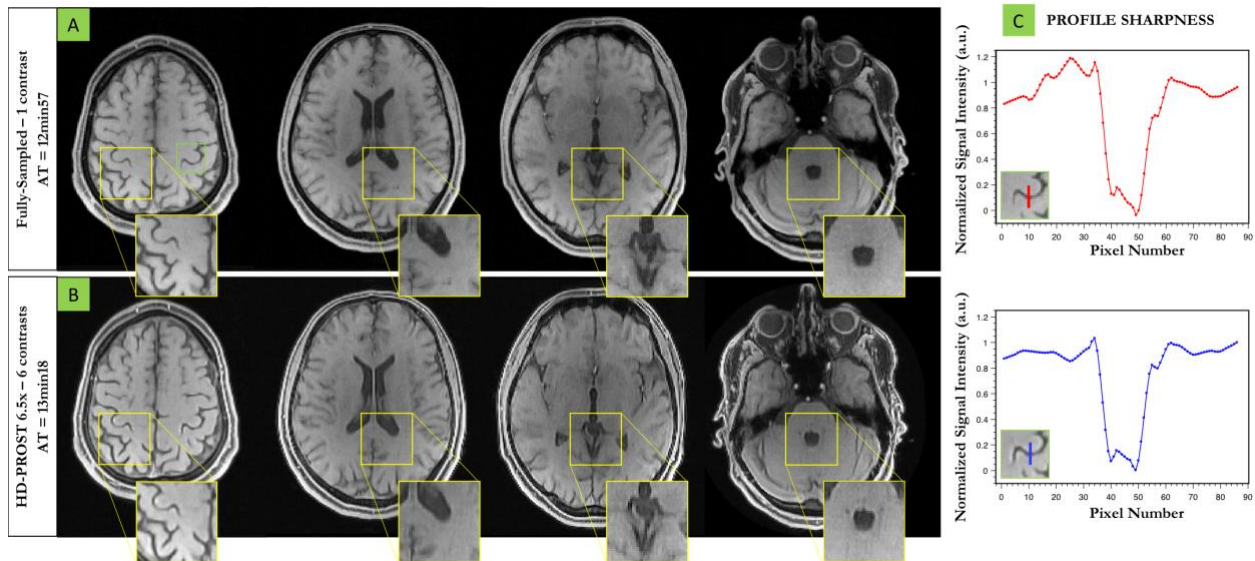


746 **Figure 5:** In vivo MRF-derived quantitative  $T_1$  (top) and  $T_2$  (bottom) maps for subject 1  
 747 reconstructed with low-rank inversion (LRI) MRF and the proposed HD-PROST  
 748 reconstruction with 2000, 1000 and 500 time-points.

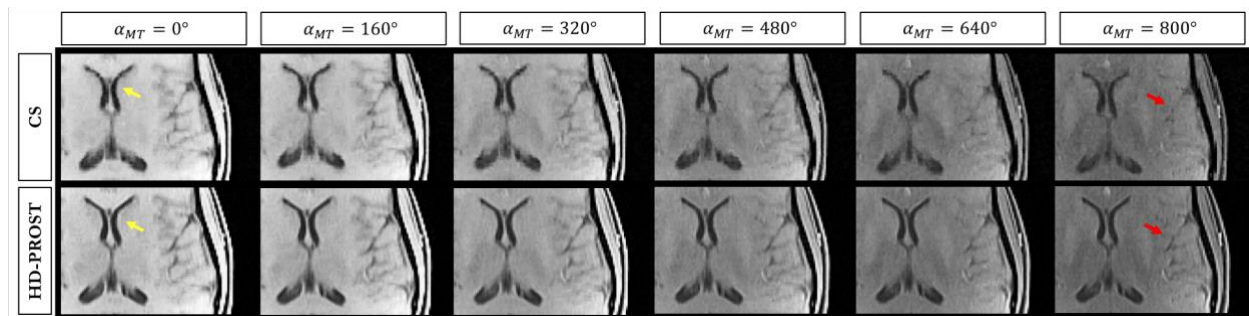
749



750 **Figure 6:**  $T_1$  (top) and  $T_2$  (bottom) maps for subject 2 reconstructed with low-rank inversion  
 751 (LRI) MRF and the proposed HD-PROST reconstruction with 2000, 1000 and 500 time-  
 752 points. The yellow and red rectangles on the top-left map indicate the regions of interest  
 753 used to determine the  $T_1$  and  $T_2$  relaxation times (see Table 1).



755 **Figure 7:** Three-dimensional reconstruction of a MT-weighted 6.5-fold undersampled  
 756 brain data in a healthy subject (subject 1). HD-PROST reconstruction (B) is compared to  
 757 the fully-sampled acquisition (A) for the reference image only ( $\alpha_{MT} = 0^\circ$ ). Line profiles  
 758 going through a structure with sharp edges are shown in (C). HD-PROST is able to recover  
 759 high fidelity 3D images and retrieve sharp edges in agreement with the fully-sampled  
 760 acquisition. Six different undersampled MT-weighted images were acquired in 13min 18s,  
 761 whereas the fully-sampled acquisition of a single contrast took 12min 57s.



763 **Figure 8:** 6.5-fold accelerated 3D MT-weighted images for 6 different contrasts from one  
764 representative subject (subject 1) reconstructed with compressed-sensing (CS), and the  
765 proposed HD-PROST reconstruction. Fine anatomical structures can be efficiently  
766 retrieved with HD-PROST as shown by the arrows. See Supporting Information Figure S5  
767 for the visualization of the whole axial images and Supporting Information Figure S6 for  
768 comparisons with zero-filling and locally low-rank reconstructions.

769

770

771

772 **Table Captions**

773 **Table 1:**  $T_1$  and  $T_2$  relaxation times at 1.5T for low-rank inversion (LRI) and the proposed  
 774 HD-PROST in regions of interest covering white and grey matters in the five healthy  
 775 subjects (regions of interest are drawn in the maps in Figure 6). Values are shown for  
 776 different MRF measurement lengths and compared with the corresponding literature values.

777

778

779

	#Time points	$T_1$ (ms)			$T_2$ (ms)		
		LRI	HD-PROST	Literature	LRI	HD-PROST	Literature
<b>White Matter</b>	2000	$737 \pm 61$	$743 \pm 37$		$45 \pm 5$	$45 \pm 4$	
	1000	$718 \pm 63$	$732 \pm 36$	608 – 756	$47 \pm 6$	$46 \pm 4$	54 – 81
	500	$741 \pm 64$	$746 \pm 44$		$42 \pm 4$	$45 \pm 3$	
<b>Grey Matter</b>	2000	$999 \pm 117$	$992 \pm 106$		$55 \pm 6$	$54 \pm 4$	
	1000	$988 \pm 125$	$982 \pm 108$	998 – 1034	$57 \pm 6$	$56 \pm 4$	78 – 98
	500	$1059 \pm 151$	$1024 \pm 128$		$52 \pm 7$	$55 \pm 4$	

780

Abbreviations – LRI: low-rank inversion, HD-PROST: high-dimensionality undersampled patch-based reconstruction. Values are expressed as mean  $\pm$  SD

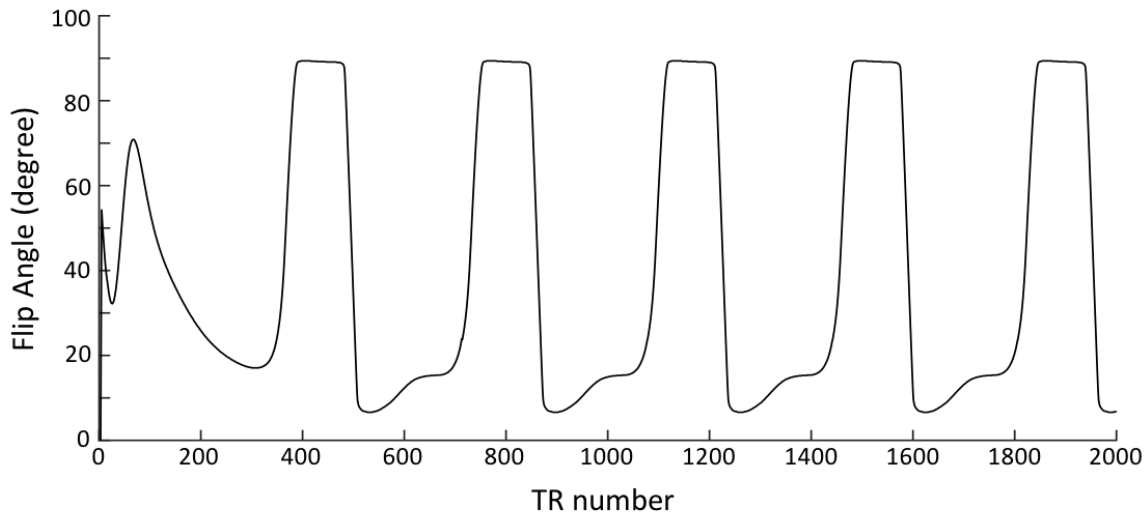
782

783

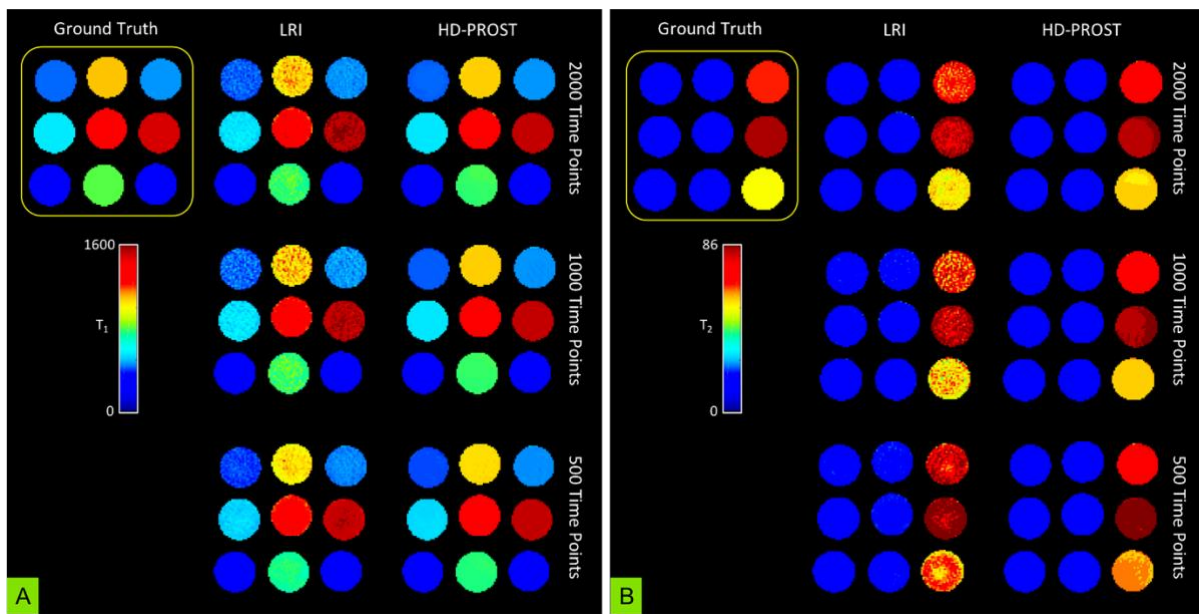
784

785

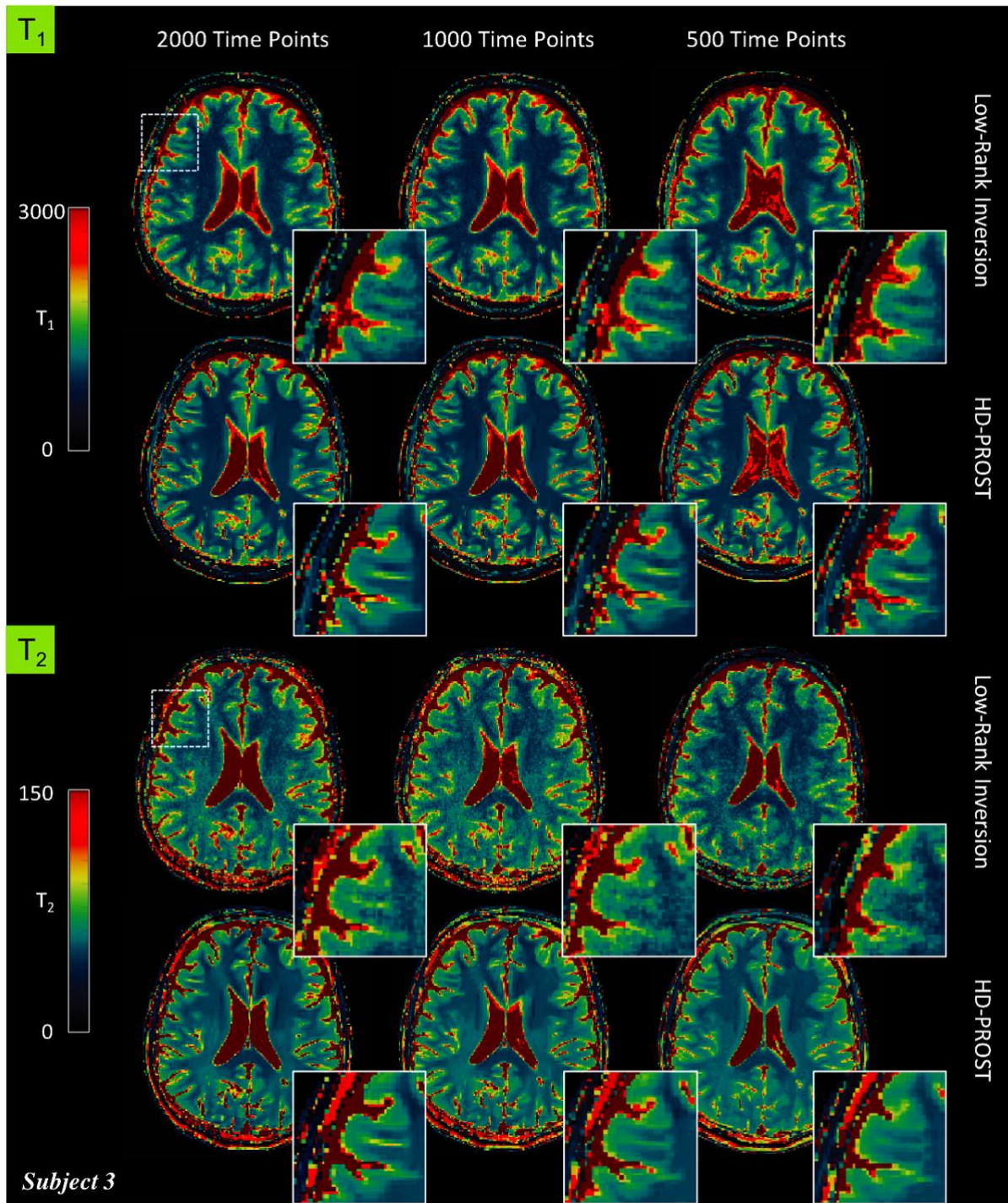


786 **Supporting Information Figure Captions**

787  
 788 **Supporting Information Figure S1:** Variable flip angle pattern used in the accelerated 2D  
 789 MRF study. This pattern was described in Assländer et al. (44).

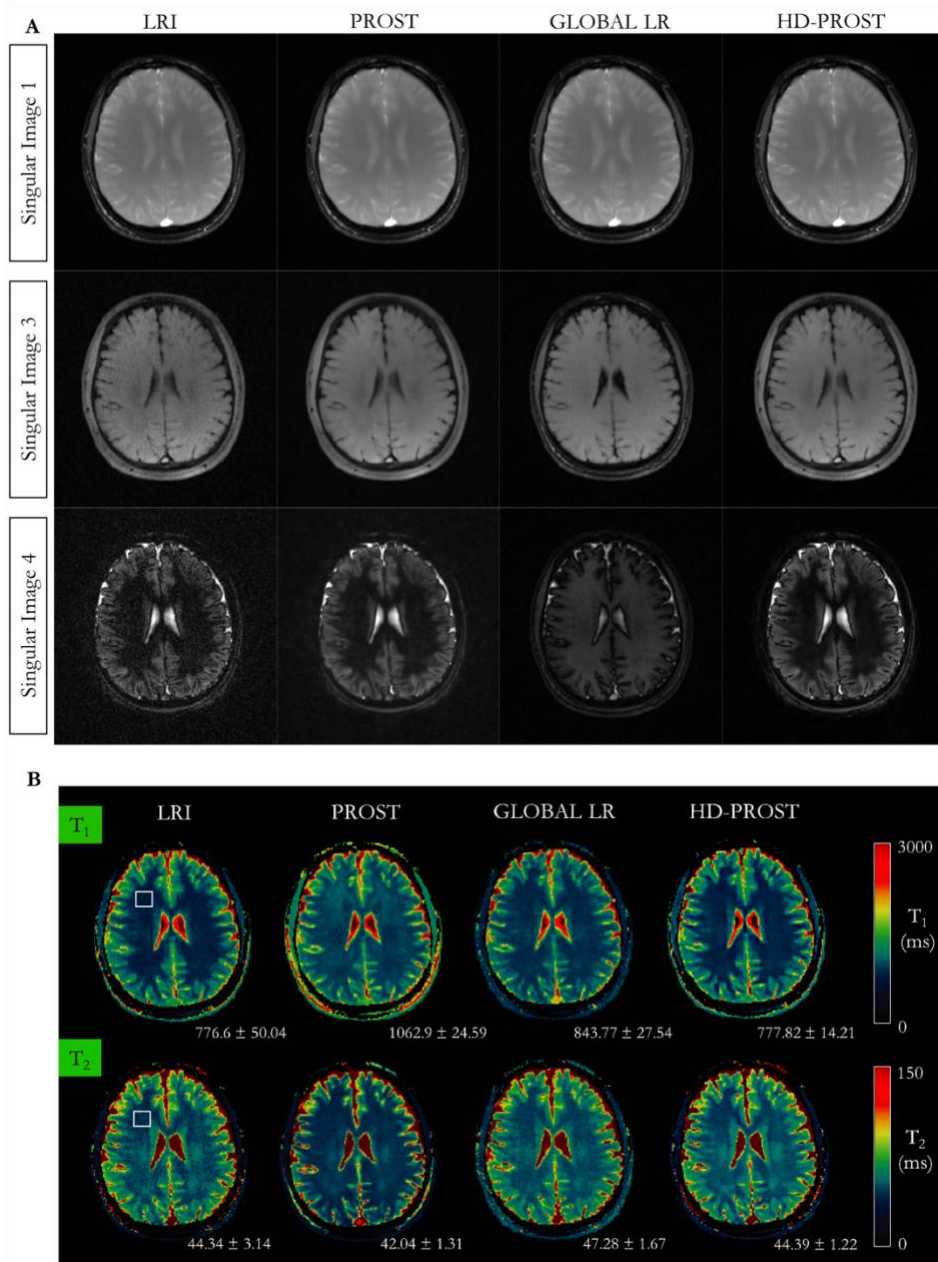


790  
 791 **Supporting Information Figure S2:** T<sub>1</sub> map (A) and T<sub>2</sub> map (B) of the 2D MRF phantom  
 792 acquisition. The quantitative values for all phantom tubes are reported in Figure 2.  
 793 Abbreviations – LRI: low-rank inversion, HD-PROST: high-dimensionality undersampled  
 794 patch-based reconstruction.



795

796 **Supporting Information Figure S3:**  $T_1$  (top) and  $T_2$  (bottom) maps for subject 3  
 797 reconstructed with low-rank inversion MRF and the proposed HD-PROST reconstruction  
 798 with 2000, 1000 and 500 time-points.

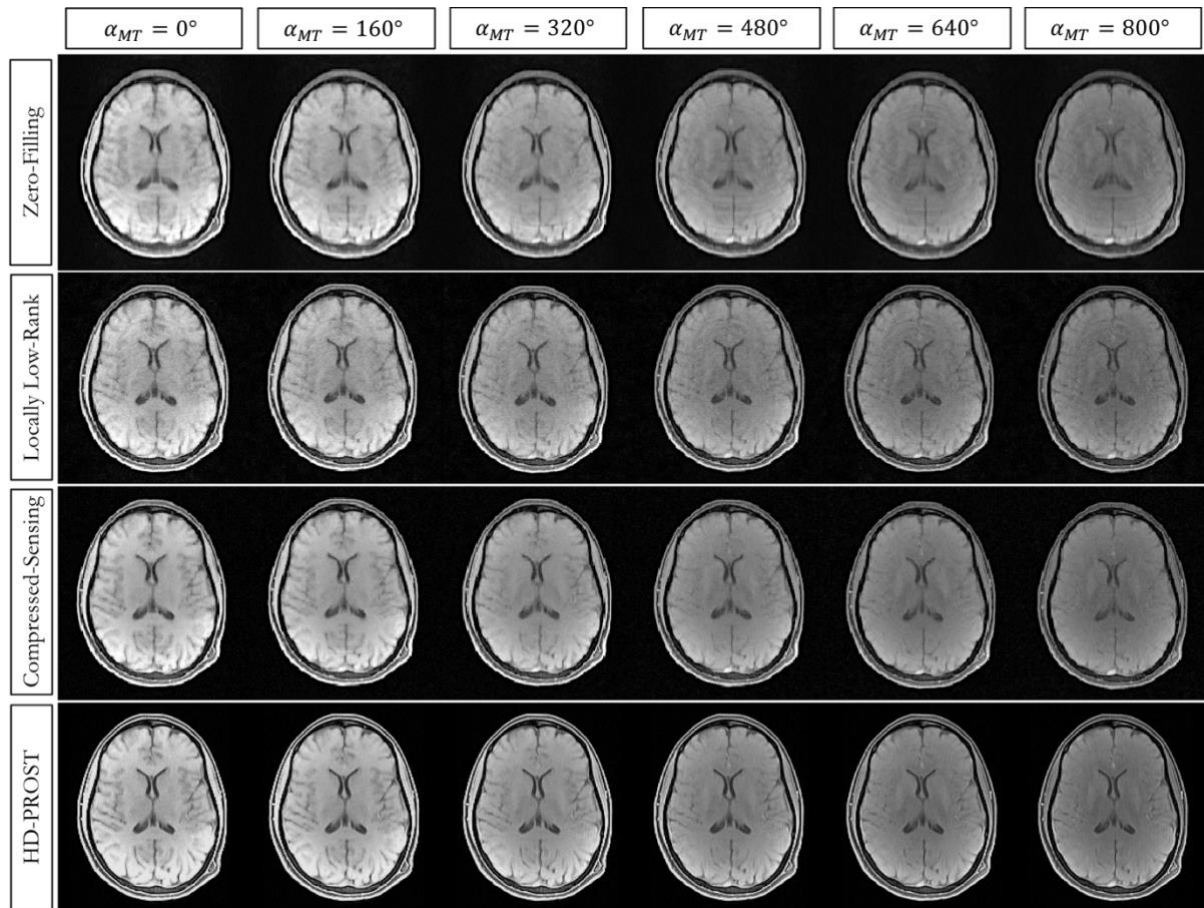


799

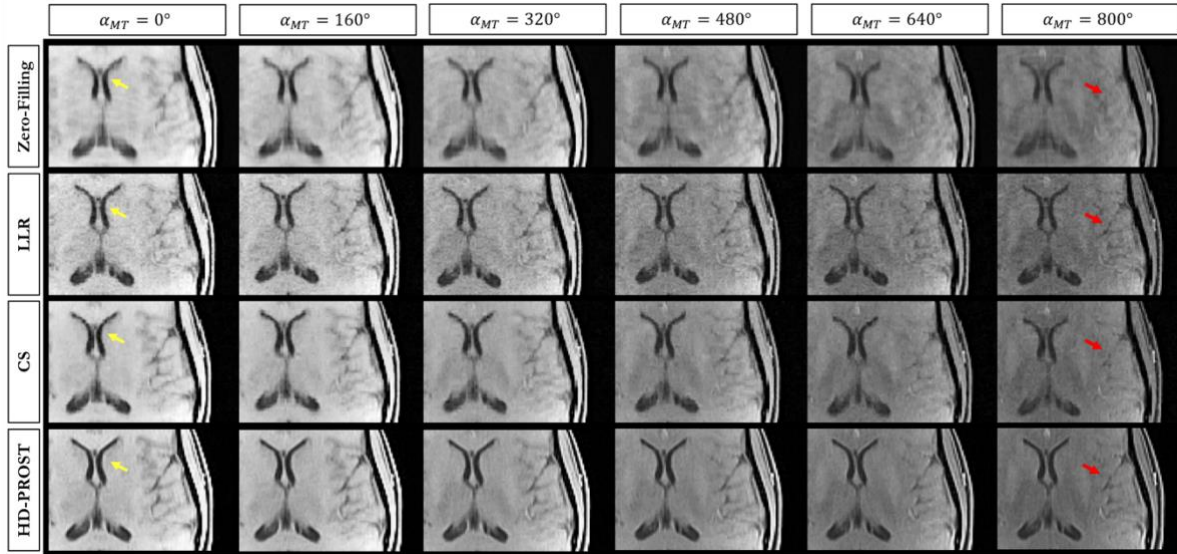
800 **Supporting Information Figure S4:** 2D MRF singular images (A) and corresponding  $T_1$   
801 (top) and  $T_2$  (bottom) maps (B) for subject 2 reconstructed with low-rank inversion (LRI),  
802 PROST (i.e. reconstructing each MRF singular image independently), global low-rank  
803 tensor decomposition (global LR) and the proposed HD-PROST reconstruction. The white  
804 rectangle on the top-left map indicates the region of interest used to determine the  $T_1$  and  $T_2$   
805 relaxation times. By exploiting local, non-local and contrast redundancies, the proposed  
806 HD-PROST technique obtains better performance than the other techniques and  
807 reconstructs high-quality  $T_1$  and  $T_2$  maps with great noise-like artefacts reduction, contrast



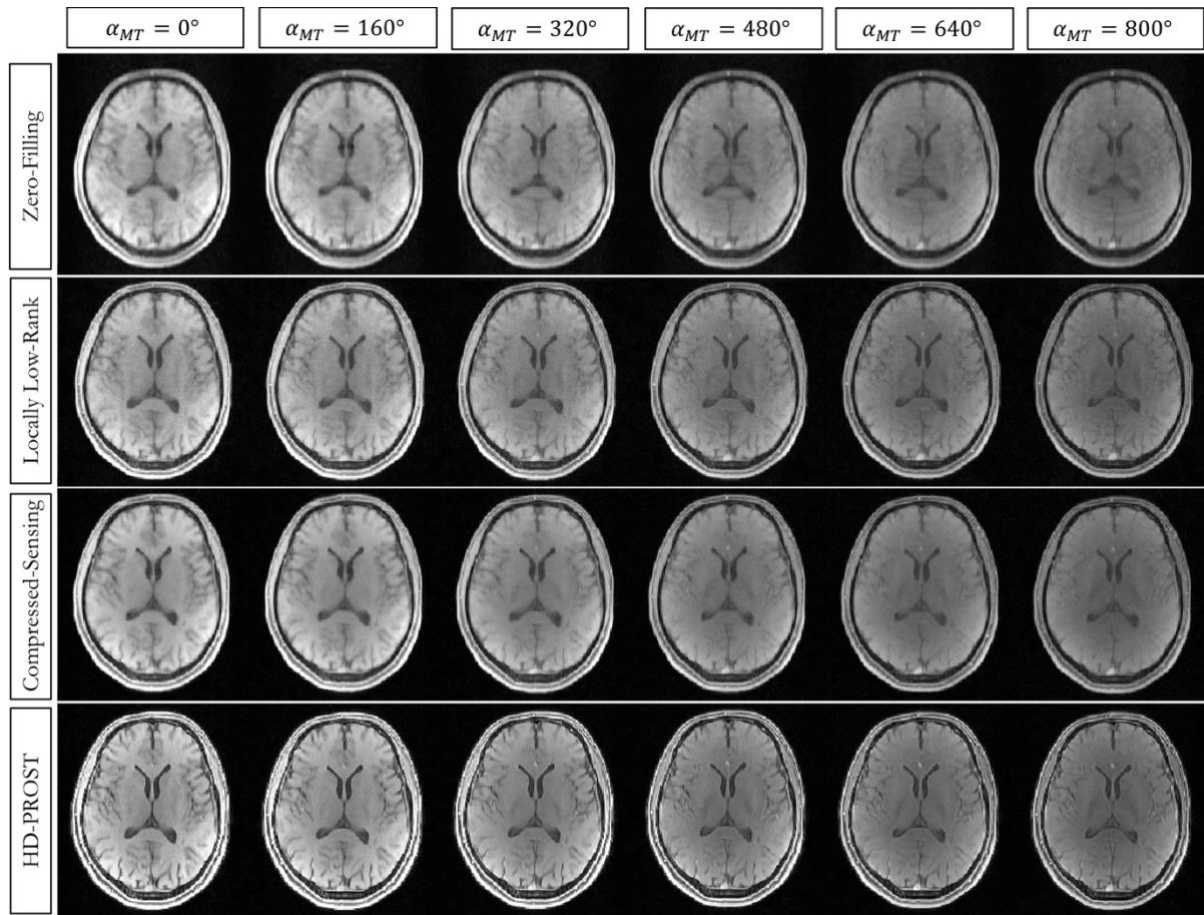
808 preservation, as well as sharpness enhancement, with  $T_1$  and  $T_2$  accuracies similar to the  
 809 unregularized LRI reconstruction.



810  
 811 **Supporting Information Figure S5:** 6.5-fold accelerated 3D MT-weighted images for 6  
 812 different contrasts from subject 1 reconstructed with zero-filling, locally low-rank,  
 813 compressed-sensing, and the proposed HD-PROST.

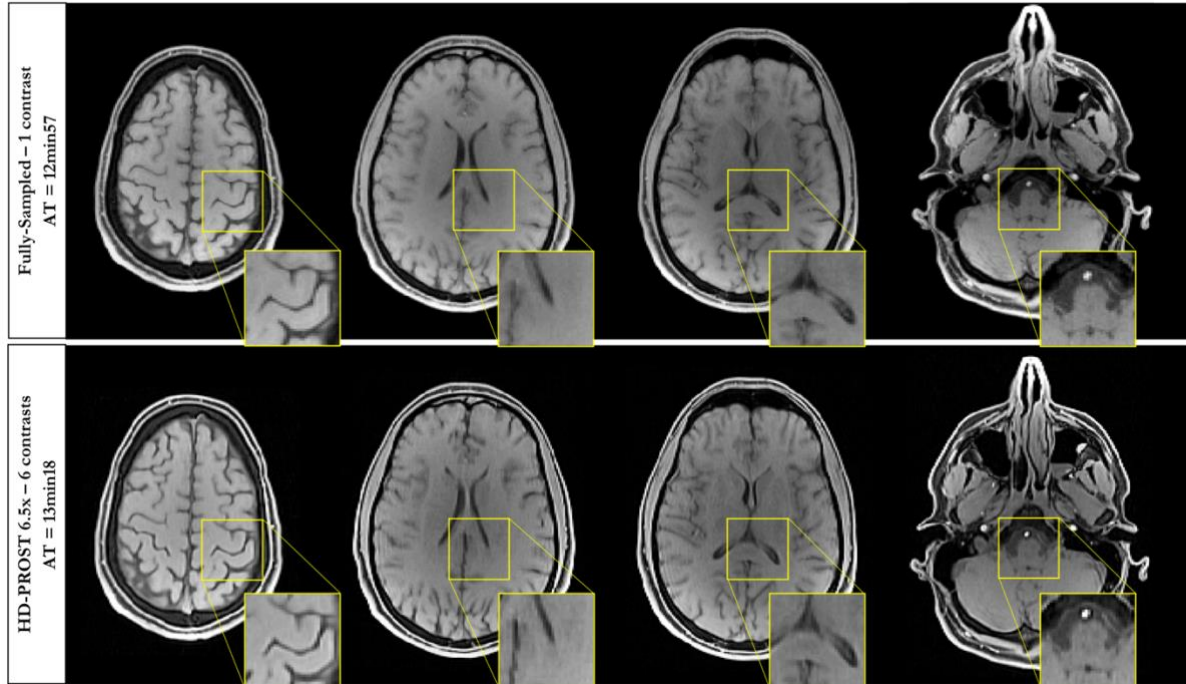


814  
 815 **Supporting Information Figure S6:** 6.5-fold accelerated 3D MT-weighted images for 6  
 816 different contrasts from one representative subject (subject 1) reconstructed with zero-  
 817 filling, locally low-rank (LLR), compressed-sensing (CS), and the proposed HD-PROST.  
 818 Fine anatomical structures can be efficiently retrieved with HD-PROST as shown by the  
 819 arrows. See Supporting Information Figure S5 for the visualization of the whole axial  
 820 images. Note that slight residual motion can be observed on the sharp HD-PROST  
 821 reconstruction, which is lost in blurring on the compressed sensing reconstruction (due to  
 822 regularization) and in the noise of LLR reconstruction.



823

824 **Supporting Information Figure S7:** 6.5-fold accelerated 3D MT-weighted images for 6  
825 different contrasts from subject 2 reconstructed with zero-filling, locally low-rank,  
826 compressed-sensing, and the proposed HD-PROST.



827

828 **Supporting Information Figure S8:** Three-dimensional reconstruction of a MT-weighted  
 829 6.5-fold undersampled brain data in a healthy subject (subject 3). HD-PROST  
 830 reconstruction is compared to the fully-sampled acquisition for the reference image only  
 831 ( $\alpha_{MT} = 0^\circ$ ). Six different undersampled MT-weighted images were acquired in 13min 18s,  
 832 whereas the fully-sampled acquisition of a single contrast took 12min 57s.

833 **Supporting Information Table Captions**

834

835

836

## ALGORITHM I

837

## HIGH-ORDER TENSOR DECOMPOSITION ALGORITHM FOR HD-PROST RECONSTRUCTION

838

839

840 **INPUT:** data tensor  $\mathcal{T}$  with dimensions  $(N, K, L)$  and regularization parameter  $\lambda$ 841 **ALGORITHM:**842 (1) Unfold the tensor  $\mathcal{T}$  along its single modes:843  $\mathcal{T}_1$ : which reshapes  $\mathcal{T}$  into a  $L \times (N \cdot K)$  complex matrix844  $\mathcal{T}_2$ : which reshapes  $\mathcal{T}$  into a  $N \times (L \cdot K)$  complex matrix845  $\mathcal{T}_3$ : which reshapes  $\mathcal{T}$  into a  $K \times (L \cdot N)$  complex matrix846 (2) Compute the complex SVD of  $\mathcal{T}_n$  and get the orthogonal matrices  $U^{(1)}, U^{(2)}, U^{(3)}$  from the  
847  $n^{\text{th}}$ -mode signal subspace848 (3) Compute the complex core tensor  $\mathcal{S}$  related by

849 
$$\mathcal{S} = \mathcal{T} \times_1 U_{(1)}^H \times_2 U_{(2)}^H \times_3 U_{(3)}^H$$

850 Which is equivalent to its unfolding forms:

851 
$$\mathcal{S}_n = U_{(n)}^H \cdot \mathcal{T}_n \cdot [U_{(i)} \otimes U_{(j)}] \text{ with } 1 \leq n \leq 3 \text{ and } i \neq j \neq n$$

852 In which  $\otimes$  denotes the Kronecker product

853 (4) Compute the high-order singular values truncation (hard-thresholding):

854 
$$\mathcal{S}(\mathcal{S} < \lambda) = 0$$

855 (5) Construct back the filtered tensor  $\mathcal{T}_{(n)}^{\text{den}}$ :

856 
$$\mathcal{T}_{(n)}^{\text{den}} = U_{(n)} \cdot \mathcal{S} \cdot [U_{(i)} \otimes U_{(j)}]^H \text{ with } 1 \leq n \leq 3 \text{ and } i \neq j \neq n$$

857 **OUTPUT:** The denoised tensor  $\mathcal{T}^{\text{den}}$  is obtained by folding

858

859

860 **Supporting Information Table S1:** Algorithm I: high-order tensor decomposition  
 861 algorithm for HD-PROST reconstruction.

862

863

864

865

866

867

---

ALGORITHM II  
 HIGH-DIMENSIONALITY UNDERSAMPLED PATCH-BASED RECONSTRUCTION (HD-PROST)

---

868 **INPUT:** *undersampled multi-channel multi-contrast images  $X$*

869 *parameters  $\lambda_p, \mu$ , ADMM iterations  $ADMM_{iter}$*

870 *Encoding operator  $E$  (coil sensitivities  $S$ , sampling mask  $A$ )*

871 *Compression operator  $U_r$  (for MRF)*

872 **INITIALIZATION:**

873 *Solve optimization 1 (Eq. 4): Joint MR reconstruction without prior ( $\mu = 0$ )*

874 *% Output:  $X^{(0)}$*

875 **ALGORITHM:**

876 *for  $i = 1, \dots, ADMM_{iter}$*

877 *Solve optimization 2 (Eq. 5): HOSVD-based denoising (see Algorithm I)*

878 *% Output: denoised tensor  $\mathcal{T}^{(i)}$*

879 *Solve optimization 1 (Eq. 4): Joint MR reconstruction with prior*

880 *% Output: reconstructed images  $X^{(i)}$*

881 *Update Lagrangian multiplier:*

882 
$$b^{(i)} = b^{(i-1)} + X^{(i)} - \mathcal{T}^{(i)}$$

883 *end for*

884 **OUTPUT:** *The multi-contrast images  $X$*

885

886

---

887 **Supporting Information Table S2:** Algorithm II: high-dimensionality undersampled  
 888 patch-based reconstruction (HD-PROST).